

Synthesis of graphenic nanomaterials by decomposition of methane on a Ni-Cu/Biomorphic carbon catalyst. Kinetic and characterization results.

F. Cazaña, N. Latorre, P. Tarifa, J. Labarta, E. Romeo, A. Monzón*

Departamento de Ingeniería Química y Tecnologías del Medio Ambiente, Instituto de Nanociencia de Aragón (INA), Universidad de Zaragoza, 50018 Zaragoza, Spain.

* Corresponding author: Tel.: +34 976 761157; e-mail: amonzon@unizar.es

Abstract

This work addresses the preparation and application of the synthesis of graphene in Ni-Cu catalysts supported on carbonaceous materials. The catalysts have been prepared by a biomorphic mineralization technique which involves the thermal decomposition, under reductive atmosphere, of commercial cellulose previously impregnated with the metallic precursors. The characterization results indicate that the preparation method leads to the formation of carbonaceous supports with a moderate microporosity (ca. 33% pore volume) and adequate surface area ($343 \text{ m}^2/\text{g}$), maintaining the original external texture. The catalytic performance of these materials was previously tested in liquid phase reactions [11]. In order to extend the use of these catalysts, in this work we present a study corresponding to a gas phase reaction: the synthesis of graphenic nanomaterials by catalytic decomposition of methane (CDM). The influence of the reaction temperature and of the feed composition (i.e. %CH₄ and %H₂) has been studied. The graphenic nanomaterials obtained after reaction were characterized by nitrogen adsorption-desorption isotherms, Raman spectroscopy and transmission electron microscopy (TEM). The results indicate that the carbonaceous nanomaterial with the highest quality is obtained operating at 950 °C and feeding 28.6% of CH₄ and 14.3% of H₂. The evolution of the carbon mass during the reaction time was analysed using a phenomenological kinetic model that takes into account the main stages involved during the formation of carbonaceous nanomaterials (NCMs). The results obtained from the kinetic model along with the characterization results enable the influence of the operating variables on each stage of the carbonaceous nanomaterial formation to be discerned.

Keywords: graphene, few layer graphene, biomorphic carbon, Ni-Cu, kinetic model, methane decomposition.

1. Introduction

Carbonaceous materials are widely used as catalysts [1] or catalytic supports [2,3] for a large variety of chemical reactions due to their textural and chemical properties: large surface area and porosity, good electrical conductivity, presence of a large variety of surface functional groups and relative chemical inertness [4]. An advantage of carbonaceous materials is that they can be prepared from renewable residual lignocellulosic biomass [3]. In this context, it has been suggested [3] that the success of processes derived from the biorefinery concept will require the design and preparation of new types of multifunctional catalysts, probably derived from emerging carbonaceous materials such as graphene (or graphene related materials), carbon nanotubes and carbon monoliths. In this context, biomimetic mineralization is one of the more interesting tools that uses the structures formed by a biological process, e.g. wood and lignocellulosic biomass, as templates for the synthesis of inorganic functional materials [5,6]. It offers the advantage of fabricating materials that are difficult to produce by top-down methods and/or have chemical compositions which cannot be produced by self-assembly [7,8]. Thus, considering that wood is a multifunctional material structured on several levels of hierarchy, a large variety of ceramic microstructured materials can be prepared using different lignocellulosic materials as templates [9]. The preparation of these kinds of materials has been carried out by thermal decomposition in a reducing (or inert) atmosphere, at high temperature and high heating rates, of several lignocellulosic raw materials (e.g. cellulose, lignin, paper, cotton, fibres, etc.) that can be previously impregnated with catalytic metallic precursors [10]. Using this technique, it is possible in a single step to obtain catalysts formed by a biomorphic carbonaceous (BC) support with the metallic nanoparticles dispersed on its surface. This method of catalyst synthesis has outstanding versatility because it allows the use of different lignocellulose raw materials with a large variety of compositions and metal contents [11].

The catalytic decomposition of methane (CDM) can be used to obtain pure hydrogen and, depending on the operating conditions selected, very high value-added carbonaceous nanomaterials such as single or multi-wall carbon nanotubes or graphene

[12,13,14]. This process can be applied in the production of CO_x free hydrogen for use, for example, in fuel cells, where the presence of CO is a poison for the electro-catalyst [15]. In this work, we use the CDM process to study the feasibility of Me/BC catalysts to synthesize specifically graphene and/or graphenic materials, such as few layer graphene (FLG) [16,17]. Nowadays, graphene and graphenic nanomaterials are attracting substantial research interest due to their exceptional properties such as high electrical conductivity, good thermal stability and excellent mechanical strength [18]. Given these properties, the use of graphene is being intensively studied for a large number of potential fields and applications such as electronics [19], photonics [20], sensors [21], catalysts [22], energy storage [23], or the manufacture of composite materials [24].

A key factor for the controlled production of graphene and graphenic nanomaterials is to understand the formation mechanism. In recent years, our research group has developed kinetic models to investigate the kinetics of growth of carbon nanotubes and carbon nanofibers [25,26,27,28,29,30,31,32]. The phenomenological models developed are based on the following steps: i) hydrocarbon decomposition over the exposed surface of the metallic nanoparticles dispersed on the support, ii) diffusion and precipitation of carbon atoms along the metallic nanoparticles, iii) nanocarbonaceous material growth, and iv) catalyst deactivation. These models have been successfully applied to study the data obtained from different reactions using different carbon sources and catalysts [25,27,31].

In this work, we present the results of graphene and FLG formation by the decomposition of methane on a catalyst of Ni-Cu supported on Biomorphic Carbon. The composition of the active phases, Ni-Cu, was chosen in order to combine the high productivity of Ni based catalysts, due to the high carbon solubility in this metal [33], and the excellent graphene quality obtained with Cu based catalyst resulting from the low carbon solubility in this metal [28,34,35]. In order to optimize the CDM process, the effect has been studied of the main operational conditions (reaction temperature, feed composition and reaction time) on the growth rate and on the quality of the graphenic nanomaterials obtained. Finally, the application of the kinetic model to analyse the data obtained in a thermobalance is discussed in the context of the reaction mechanism.

2. Experimental

2.1 Materials

The raw material used to prepare the biomorphic catalyst was cellulose provided by Sigma Aldrich (ref: C6288). The metal precursors used were Ni (II) nitrate hexahydrate supplied by Alfa Aesar (ref: 10816) and Cu (II) nitrate hydrate provided by Sigma Aldrich (ref: 61194).

2.2 Catalysts preparation

For the preparation of the Ni-Cu/Biomorphic carbon catalyst, the cellulose was dried at 100 °C overnight and then impregnated by incipient wetness with the appropriate amounts and concentrations of Ni and Cu aqueous solutions. After impregnation, the solid was dried at 80 °C overnight and then thermally decomposed in a reducing atmosphere (15% H₂, 85% N₂) at 800 °C during 75 minutes. The decomposition temperature was reached at a heating rate of 42 °C/min. Finally, the catalyst was milled and sieved to obtain a homogeneous particle size distribution, ranging between 80 to 200 micrometres, and stored under N₂ atmosphere.

2.3 Catalytic decomposition of methane

The CDM reaction was carried out at atmospheric pressure in a thermobalance (CI Electronics Ltd., UK, model MK2) operated as a differential reactor (i.e. methane conversions less than 10%), and equipped with mass flow and temperature controllers. This experimental system allows continuous recording of the variations of sample weight and temperature during reaction. The reaction conditions were as follows: sample weight: 25 mg; total flow-rate: 700 N mL/min.; temperature range: 850-975 °C; feed composition range: %CH₄: from 1.4% to 42.9%, %H₂: from 0% to 28.6% and N₂ until balance; reaction time: from 1 to 120 minutes.

2.4 Catalysts and carbonaceous nanomaterials characterization

The catalysts and carbonaceous nanomaterials were characterized in order to know their textural and structural properties and the type of carbon structures formed (e.g. graphene, few layer graphene (FLG), graphite, etc.). The thermogravimetric analyses in

air (TGA-Air) were carried out with a Mettler Toledo TGA/SDTA 851 analyser, using 50 mL/min. This technique allows the calculation of the amount of Ni and Cu deposited on the biomorphic carbon support after the thermal decomposition of the cellulose. After the combustion in the TGA-Air experiment the solid residue consists of NiO, CuO and ashes. Knowing the initial amount of Ni and Cu, the final percentage of each component can be calculated. This protocol was repeated three times with each carbonaceous catalyst in order to determine the variability of this procedure. Specific area and porosity were obtained from nitrogen adsorption–desorption isotherms at 77 K using a TriStar 3000 instrument (Micromeritics Instrument Corp.). BET specific surface areas were measured from the adsorption branches in the relative pressure range of 0.01-0.10. The micropore volume estimation was made by means of the *Dubinin-Radushkevich* method [36].

The X-ray diffraction (XRD) patterns were recorded within the range of 5-90° (2 θ) with a Rigaku D/Max 2500 apparatus operated at 3.2 kW (40 kV, 80 mA) and with a rotatory anode of Cu using Cu K α radiation. For the graphenic materials formed during the reaction, the crystallite size along the c-axis, L_c , and the interlaminar distance, d_{002} , were obtained from the (002) reflection at 2 θ =26° of the XRD patterns [37]. From this value, the number of graphene layers of each sample, n , was calculated as: $n=(L_c/d_{002})+1$ [38,39].

Transmission electron microscopy (TEM) micrograph images were recorded in a FEI Tecnai T-20 microscope, operated at 200 kV. Scanning electron microscopy (SEM) micrograph images were captured in a FEI Inspect F50 microscope, operated at 10 kV. The carbonaceous nature of the catalyst support and of the materials formed during the reaction was characterized by Raman spectroscopy using a WiTec Alpha300 Confocal Raman Microscope, with a 532 nm laser excitation beam.

3. Results and discussion

3.1 Characterization of fresh catalyst

The Ni-Cu/BC catalyst was prepared with nominal contents (*wt. %*) of 5% Ni and 1% Cu regarding to the initial amount of cellulose. After preparation, the final amounts of metal, calculated from the TGA-air data, were ca. 40% and 8% with in relation to the

final amount of biomorphic carbon formed. Replicated TGA measurements gave metal composition values with variations of less than 3%, confirming the validity of this procedure. Obviously, due to the loss of carbonaceous material during the thermal decomposition stage, the weight percentages of Ni and Cu are substantially increased (8 times in this case) in the final catalysts. In fact, the thermal decomposition is a key factor for controlling the final content and dispersion of the metal(s) on the surface of the catalyst.

Figure 1 shows the N₂ adsorption/desorption isotherm for the Ni-Cu/BC catalyst. According to the IUPAC classification, the isotherm corresponds to I- and II-types, with a hysteresis loop of type H3 or H4 [40,41]. These types of hysteresis loops are characteristic of disordered materials containing aggregates of plate-like particles forming slit-shaped pores [41]. In addition, the adsorption/desorption results, shown in Table 1, give a BET value of 343 m²/g and 33% of micropore volume. Usually, the percentage of the micropore volume in this kind of support is quite high (above 70%) [11]. However, in this case, due to the large size of the metallic nanoparticles formed (see TEM results in Figure 3b), a significant part of the micropores, about half, are blocked and the resulting value is lower.

Figure 2 shows the XRD patterns of the Ni-Cu/BC. It is observed that the three peaks appearing at 44.3°, 51.6° and 76.0° do not correspond to the metallic Ni or Cu patterns. In addition, the Ni-Cu/BC pattern does not show any peak associated to the presence of NiO or CuO, indicating that the catalyst is completely in the reduced state. According to Wu et al. [42], the shift observed in the 2θ value for these peaks can be attributed to the formation of a Ni-Cu alloy. In fact, according to Vegard's law [43], the peak observed at 44.26° corresponds to a Ni-Cu alloy with an atomic ratio of Ni/Cu=1/6, consistent with the nominal catalyst composition. On the other hand, in the case of the Ni-Cu/BC sample before reaction, the absence of the peak at 26° corresponding to the (002) diffraction of the graphitic structures [37,44] indicates that carbonaceous material formed during the preparation of the catalyst is poorly crystallized and the presence of any graphitic structure is not observed.

Figures 3a and 3b show respectively the SEM and TEM images of the fresh catalyst. The macrostructure and smoothness characteristic of this kind of carbonized material can be seen in Figure 3a [45]. Interestingly, some of the Ni-Cu particles are clearly

visible due to the large size attained by some of them during the preparation. The microstructure of the catalyst observed in the SEM and TEM images in Figure 3 indicates that the metallic particles are spread all over the support. However, the size distribution is quite heterogeneous, with some quite small particles (~ 5 nm) and others very large (> 50 nm), resulting in a low dispersion of the active phase. The TEM image also clearly shows the characteristic microporosity of the support.

The Raman result for the Ni-Cu/BC catalyst, see Figure 4, is characteristic of this type of material [46], presenting two broad peaks at about 1350 cm^{-1} (D band) and 1590 cm^{-1} (G band), these being the consequence of several contributions [46]. The characteristic ratio I_G/I_D , related to the type and number of defects [47], obtained for this catalyst is about 1.03, which is quite similar to those obtained for a Pd-Al/CB [11], indicating that although some textural properties of the support are affected (e.g. microporosity), the type of metal used has low influence on their structural features.

3.2 Characterization of carbonaceous nanomaterials grown

In order to know the effect of the reaction temperature, the feed composition and the reaction time on the quality of the carbonaceous nanomaterials grown, the samples obtained after each reaction test were analysed by nitrogen adsorption–desorption isotherms at 77 K, Raman spectroscopy and transmission electron microscopy. In addition, the amount of carbon produced was obtained directly from the thermobalance measurements. With the aim of evaluating the catalytic activity of the support without metal, repeated experiments at 950 °C, 28.6% CH₄, 14.3% H₂ and 57.1% N₂ were carried out. In all cases an almost negligible activity was found, as corresponds to the low carbon formation observed (below 0.03 gC/gCat). In addition, the Raman, XRD and TEM results (not shown) after these experiments confirm that there is neither formation of appreciable amounts of carbon, nor substantial modification of the textural and structural properties.

3.2.1 Influence of the reaction temperature

Figure 1 also shows the N₂ adsorption/desorption isotherms for the catalyst after reaction at 900, 950 and 975 °C. As in the case of the fresh catalyst, these isotherms correspond to I- and II-types, with hysteresis loops of type H3 or H4 [40,41]. However, as can also be seen in Table 1, the BET surface area and the pore and micropore

volumes are strongly modified, all of them decreasing as the reaction temperature increases. Moreover, the % of micropore volume is also reduced, showing that the carbon formed during the reaction mainly blocks the micropores of the support.

The Raman spectra acquired for the samples obtained at different reaction temperatures are shown in Figures 4a and 4b. The feed composition used for these experiments was 28.6% CH₄, 14.3% H₂ and 57.1% N₂. In addition, Table 2 includes the values of the ratios I_G/I_D and I_{2D}/I_G calculated from the spectra. In all cases, see Figure 4a, a peak appears at about 2690-2700 cm⁻¹, the 2D band, characteristic of graphenic materials [48,49].

From the values of the I_G/I_D and I_{2D}/I_G ratios presented in Table 2 and in Figure 4, it can be deduced that the quality of the carbonaceous nanomaterials formed is clearly dependent on the reaction temperature and, in general, on the operating conditions during the CDM.

Thus, the I_G/I_D ratio decreases from 3.31 to 1.0 as the temperature increases from 850 to 975 °C. On the other hand, the I_G/I_{2D} ratio, related to the number of layers of graphene [50,51], reaches a maximum of 0.92 at 950 °C, decreasing until 0.69 at 975 °C. According to Hao et al. [50] and Cong et al. [51], the material obtained at 950 °C mainly corresponds to FLG (2 or 3 layers), while at 900 °C and 975 °C the I_{2D}/I_G ratio would indicate the formation of graphite and/or FLG with more layers. These results are corroborated by the deconvolution of the 2D band, shown in Figure 4b. The 2D is an overtone of the D band, and its position and FWHM depends on the number of layers of the graphenic material [16,52]. According to Ferrari et al. [16], the 2D band has four components centred at 2660 cm⁻¹ (2D_{1B}), 2684 cm⁻¹ (2D_{1A}), 2700 cm⁻¹ (2D_{2A}) and 2722 cm⁻¹ (2D_{2B}), being the relative intensities of the bands 2D_{1A} and 2D_{2A}, higher than the 2D_{1B} and 2D_{2B}. An increase in the number of layers causes a significant decrease in the relative intensity of the lower frequency 2D₁ peaks. From the total intensity of the 2D band, and the relative distribution of intensities of these four peaks, the number of layers in the graphenic materials can be estimated. From the results in Figure 4b and from the ratios I_{2D}/I_G, it can be estimated that at 950 °C the number of layers is 2 or 3, and at 900 °C the number of layers is higher than 5, obtaining even graphite layers [16].

Figures 5a and 5b show the representative TEM images obtained after reaction using a feed composition of 28.6% CH₄, 14.3% H₂ and 57.1% N₂ carried out at 900 and 950 °C,

respectively. At 900 °C, the image shows that the carbon formed is mainly made up of graphite nanolayers of around 20-30 nm thickness, covering the exposed surface of the metallic particles. Furthermore, in agreement with the Raman results, at 950 °C (see Figure 5b) the formation of graphene flakes and/or FLG is clearly observed. However, at this temperature the presence of metallic nanoparticles covered by graphite nanolayers is also observed (not shown).

3.2.2 Influence of the partial pressure of methane

Figure 6 shows the Raman spectra corresponding to the experiments carried out at 950 °C and at different concentrations of methane (14.3% H₂ constant in all experiments) and of the fresh catalyst. After reaction, in all cases the 2D band at ca. 2690 cm⁻¹ is observed, indicating the formation of carbonaceous nanomaterials of graphenic character [48]. In addition, the separation of the bands D and G is clearer, and the intermediate peak between both bands has almost disappeared. However, at low partial pressure of methane (1.4%), the shape of the D and G bands indicates that the coverage of the support surface is incomplete. In Table 2 it can be seen that the ratio I_G/I_D attains a maximum of 6.5 for 7.1% of CH₄, but for the I_{2D}/I_G ratio the maximum value of 1.68 is observed for the experiment at 14.2% of CH₄. According to Cong et al. [51], these values indicate that the graphenic material formed corresponds to FLG containing 2 or 3 layers with low structural defects. Finally, operating at high methane contents, i.e. 42.9%, there is an increase in the D band and a diminution in the 2D band, indicating the formation of graphite layers with structural defects. Therefore, there is an optimum concentration of methane in the feed, placed between 7% and 14%, that maximizes the formation of graphenic materials.

Figure 7 shows the representative TEM images of the samples after reaction at 950 °C and at different partial pressures of methane (14.3% H₂ constant in all experiments). At low partial pressures (7.1%), the image shown in Figure 7a indicates that the predominant carbonaceous species are graphite nanolayers of ca. 40 nm thickness, surrounding the metallic nanoparticles. Under these conditions, the presence of graphene or even FLG is not observed in any of the images. In accordance with the Raman results, as the partial pressure of methane increases, the quality (i.e. the content of FLG and/or graphene) of the material obtained is enhanced. Thus, for 28.6% of methane the TEM images (Figure 7b) show clearly the formation of graphene flakes.

Besides, under these experimental conditions FLG and lower contents of graphite nanolayers are also detected. At high partial pressures (42.9% CH₄, Figure 7c) the carbon formed is mainly composed of graphite nanolayers around the metallic particles. Besides, in some images (not shown here) the presence of minor amounts of FLG was also observed. In summary, the TEM results also confirm the existence of an optimum methane concentration at which a higher proportion of graphene and FLG is obtained in the carbonaceous nanomaterials.

3.2.3 Influence of the partial pressure of hydrogen

As in the case of the temperature and the %CH₄, Table 2 and Figures 8 and 9 present the Raman and TEM results obtained in the study of the influence of the hydrogen concentration in the feed. These experiments were carried out at 950 °C and with 26.8% of methane. The Raman results in Table 2 and Figure 8 indicate that as the hydrogen content increases, the number of defects in the carbon formed diminishes, and therefore the I_G/I_D ratio decreases. Simultaneously, the I_{2D}/I_G ratio increases until attaining a value of around 0.9 at the higher concentrations tested. The formation of graphene flakes and/or FLG after reaction with 14.3 % of H₂ can be seen in Figure 9b. In contrast, in the absence of hydrogen (see Figure 9a) the nanomaterial grown is mainly formed by graphite with a large number of structural defects (I_G/I_D=1.16). Furthermore, some images (not shown here) also revealed the formation of carbon nanofibers with diameters of around 100 nm and a length of 1 micron, in accordance with the intensity of the D band measured in the Raman spectra (Figure 8). In summary, the presence of hydrogen is beneficial for obtaining high quality graphenic nanomaterials.

3.2.4 Influence of the reaction time

Figure 10 shows the evolution of the Raman spectra of the fresh catalyst, i.e. at reaction time = 0, and after 1, 4 and 120 minutes of reaction at 950 °C, 28.6% CH₄ and 14.3% H₂. Table 2 shows the values of the I_G/I_D and I_{2D}/I_G ratios calculated for each case. These results indicate that after 1 minute of reaction, the metal nanoparticles are partially covered by graphite (e.g. I_{2D}/I_G = 0.24). Graphene, FLG or other carbonaceous nanomaterial are not detected in any spectrum acquired for this sample. Also, the width of the D and G bands indicates that most of the Raman signal comes from the biomorphic carbon support. After 4 minutes of reaction, an increment in the I_{2D}/I_G ratio is observed; and finally, after 120 minutes, the I_{2D}/I_G ratio reaches a value of 0.92. As

has been discussed, this value corresponds to the presence of FLG. In addition, the lower width of the D and G bands indicates a decrease in the structural defects of the graphenic material grown, indicating the almost complete coverage of the biomorphic carbon support by sheets of the graphenic material.

The TEM images presented in Figure 11 show that after 1 minute of reaction some of the metallic nanoparticles are already coated with a continuous layer of graphite with a thickness of about 30 nm (see Figure 11a). In this Figure it can be observed that the graphite layer is partially separated from the particle on which it was generated, which could facilitate its exfoliation and the diffusion of CH₄ and H₂. After 4 minutes or reaction (Figure 11b), an increase in the thickness of the graphite layer and a higher separation from the metal particle is observed. Finally, after 120 minutes (Figure 11c) the growth of graphene flakes and FLG can be seen, in agreement with the Raman results. Other TEM images of this sample taken at this time (not shown) demonstrate the presence of partially exfoliated carbonaceous material, which will lead to the formation of separated layers of graphene and FLG.

It can be seen in Figure 2 that after reaction, the formation of graphitic structures is evident, with the characteristic XRD peaks appearing at 26° (200) and 43° (100). As expected, the intensity of these peaks increases during the reaction time as a consequence of the accumulation of graphitic material over the surface of the catalyst. As indicated in the Experimental Section, the evolution over time of the graphitic crystal size, L_C , and the number of layers has been estimated from the XRD patterns shown in Figure 2 [37,38,39]. Thus, after 1 minute of reaction, the number of graphene layers estimated is 25 and $L_C=8.2$ nm; after 4 minutes, $n= 31$ layers and $L_C=10.2$ nm; and finally, after 120 minutes, $n= 28$ layers and $L_C=9.1$ nm. These values confirm the TEM and Raman results, all of which indicate that after ca. 4 minutes, the graphitic nanolayers surrounding the metallic nanoparticles are already developed. From this point an “in-situ” exfoliation of these layers occurs to form the flakes of graphene and FLG. In addition, the average diameter of the Ni-Cu particles remains constant over time. This value is similar to that obtained for the fresh catalyst, ca. 44 nm, indicating that there is no additional sintering of the metallic phase phenomenon during the reaction.

3.3 Kinetic study and modelling of the carbonaceous nanomaterials growth.

In addition to the characterization results, a complete set of experiments has been carried out in order to measure the productivity of the Ni-Cu/BC catalyst and the influence of the main operating variables during the decomposition of methane. In order to accomplish a quantitative description of the kinetics reaction, we have applied a phenomenological model [29,31,53,54] that takes into account the main stages involved in the carbonaceous nanomaterial formation. Briefly, the reaction mechanism can be described by the following steps: *i*) adsorption and decomposition of methane on the gas side of the metallic nanoparticles; *ii*) reaction of carbon atoms with the surface of the metallic nanoparticles, forming a metastable carbide which, under the reaction conditions, decomposes leaving carbon atoms at the metallic subsurface; *iii*) diffusion and precipitation of carbon atoms forming the graphite nanolayer covering the metallic nanoparticle (see Figure 11a); *iv*) exfoliation of graphite nanolayers due to the action of the reaction atmosphere. After this step the formation of separate sheets of graphene and FLG can be observed (see Figure 11c). The final step is *v*), the catalyst deactivation. The causes of the decay of the catalyst activity can be related to all the complex phenomena involved during the diffusion of the reactants through the layers of graphite, the reconstruction and encapsulation of the metallic nanoparticles during the reaction, and the steric hindrance to the growth of graphitic nanomaterials in the form of layers [29,31]. The necessary complexity of a rigorous mathematical description of these phenomena, in addition to those involved in the previous stages of the reaction, usually results in the use of simplified models that are nevertheless very useful for optimising the production process of the materials.

As regards the kinetics results, Figures 12a, 12b and 12c show the influence of the temperature, partial pressure of CH₄ and partial pressure of H₂, respectively. These curves show the evolution of the carbon concentration (m_c), expressed as gC/gcat, with time under the experimental conditions studied. The reaction rate is calculated as the numerical derivative of the m_c vs. *time* data. The catalyst productivity is estimated as the average reaction rate for a given interval of time. Table 2 includes the data of the average catalyst productivity obtained at the end of each experiment.

In this case we have calculated the quotient between the values of carbon concentration and time and the end of reaction.

In all cases the shape of the curves is similar, with a high initial slope corresponding to a high reaction rate. Gradually, the rate decreases until reaching a final value corresponding to the almost linear increase of the m_C vs. *time* curves.

As expected, the changes in the operating conditions modify the reaction rates and the evolution of the curves. In particular, the increase in the reaction temperature from 850 to 975 °C, see Figure 12a, causes an increase in the initial reaction rate, and an increase in the final amount of carbon produced and therefore of the catalyst productivity. However, as can be seen in Table 2, the increase in the catalyst productivity at high temperatures, 0.0146 gC/gcat·min at 975 °C, causes a loss in the carbon quality as the I_G/I_D and I_{2D}/I_G ratios indicate. In Figure 12b it can be seen that the effect of the increase in the methane concentration, from 1.4 to 42.9%, is qualitatively similar, observing again that the higher productivities attained, 0.0146 gC/gcat·min at 42.9% of CH₄, are accompanied by a decrease in the selectivity to the desired carbonaceous nanomaterials. In contrast, the increase in the % of hydrogen, see Figure 12c, has a low effect on the initial rate, but causes a continuous decrease in the catalyst productivity. In summary, it can be inferred from the data in Table 2 that the optimal operating conditions which combine high productivity and sufficient carbon quality are around 950 °C, 28.6% of CH₄ and 14.3% of H₂.

3.3.1 Development of the kinetic growth model

The reaction rate, i.e. the rate of carbon production, $(r_C)_t$, is defined by the following expression [31,53,54]:

$$(r_C)_t = \left(\frac{dm_C}{dt} \right)_t = (r_C)_0 \cdot a(t) = j_{C_0} \cdot \theta_S(t) \cdot a(t) \quad \leftrightarrow \quad a(t) = \frac{(r_C)_t}{(r_C)_0} \quad (1)$$

In this equation, m_C represents the carbon concentration accumulated over the catalysts, expressed as gC/gcat; j_{C_0} has units of (gC/gcat·min) and can be considered as the intrinsic carbon growth rate for the fresh catalyst. This parameter depends on the carbon solubility and diffusivity, which determine the driving force for the diffusion of the carbon atoms through the metallic nanoparticles [31]. The term $\theta_S(t)$ is the degree of carburization of the surface of the metallic nanoparticles, and $a(t)$ is the remaining catalyst activity. As shown in equation (1), the activity is defined as the observed

reaction rate at a given time, divided by the reaction rate in the absence of any deactivation process [54,55].

According to the reaction mechanism described, the formation of the metastable surface carbide is a key step in the reaction [56]. It is assumed that the carburization process follows an autocatalytic kinetics [29,31] and the degree of carburization growth with the time from 0 to 1. The delay caused by the initial carburization of the metallic nanoparticle is responsible for the appearance of a period of induction, where the reaction rate is very low giving the carbon growth curves a sigmoidal shape [31]. However, in the present case the period of induction is not observed because the carburization step is very fast due to the high temperatures used during the reaction. Then, we can assume that $\theta_s = 1$ from the beginning of the reaction and consequently $(r_c)_0 = j_{c_0}$.

Finally, the evolution over time of the carbon content can be calculated by the integration of equation (1). Considering that the term j_{c_0} is constant, the expression obtained is:

$$m_c(t) = \int_0^t j_{c_0} \cdot \theta_s \cdot a \cdot dt = j_{c_0} \cdot \int_0^t a \cdot dt \quad ; \quad \theta_s = 1 \quad (2)$$

In order to solve this equation, it is necessary to know the kinetics of the catalyst deactivation. Given that the experimental results shown in Figure 12 indicate the presence of a residual reaction rate, we have tested several models for the catalyst deactivation that take into account the existence of residual activity [31,57]. The deactivation model selected provides the following deactivation rate, r_d : , [57]:

$$r_d = -\frac{da}{dt} = \psi_d \cdot a - \psi_r \cdot (\sqrt{a} - a) \quad (3)$$

The selection of this deactivation equation has been made considering the best fitting of all the data presented in Figures 12a, 12b and 12c. In equation (3), the parameters ψ_d and ψ_r are the kinetic functions of deactivation and regeneration, respectively. Both have dimensions of time^{-1} and, for a given catalyst, depend on the experimental conditions used during the reaction. The parameter ψ_d , is determined by the loss of catalyst activity, and the regeneration term, ψ_r , accounts for the residual rate of reaction

which will be 0 in the case of complete deactivation of the catalyst. The analytical solution of equation (3) is:

$$a = \left(\frac{\psi_r}{\psi_G} + \frac{\psi_d}{\psi_G} \cdot \exp\left(-\frac{\psi_G}{2} \cdot t\right) \right)^2 \quad (4)$$

where the term ψ_G is: $\psi_G = \psi_d + \psi_r$. After substitution of equation (4) in equation (2) and integration, the explicit function that gives the evolution of the carbon content with time is obtained:

$$m_C = j_{C_0} \cdot \left(\frac{\psi_r}{\psi_G} \cdot t + \tau_{m_1} \cdot (1 - \exp(-\psi_G \cdot t)) + \tau_{m_2} \cdot \left(1 - \exp\left(-\frac{\psi_G}{2} \cdot t\right) \right) \right) \quad (5)$$

The terms τ_{m_1} and τ_{m_2} are parameters related to the characteristic deactivation and regeneration times, defined by:

$$\tau_{m_1} = \frac{\psi_d^2}{\psi_G^3} \quad ; \quad \tau_{m_2} = \frac{4 \cdot \psi_d \cdot \psi_r}{\psi_G^3} \quad (6)$$

The model resulting from equation (5) predicts a constant residual rate, but the experimental results of Figure 12 do not strictly follow this behaviour. The final part of the experiments has a curvature which is a consequence of a detrimental loss of the reaction rate. This has been included in the model by introducing a new parameter, n , as a power of the first linear term of equation (5). Finally, the final expression for the kinetic model is given by:

$$m_C = j_{C_0} \cdot \left(\frac{\psi_r}{\psi_G} \cdot t^n + \tau_{m_1} \cdot (1 - \exp(-\psi_G \cdot t)) + \tau_{m_2} \cdot \left(1 - \exp\left(-\frac{\psi_G}{2} \cdot t\right) \right) \right) \quad (7)$$

Given the experimental results presented in Figure 12, it is presumed that the values of n will be in the interval $0 < n < 1$. The smaller the power n , the lower the residual rate, and in the case of $n = 1$, the residual rate will be constant and equal to the following asymptotic value:

$$(r_C)_s = j_{C_0} \cdot \frac{\psi_r}{\psi_G} \quad (8)$$

The physical meaning of this parameter is under discussion, but it could be related to the diffusional restrictions on the methane to attain the surface of the metallic

nanoparticles which are surrounded by the growing layers of graphite. Obviously, these diffusional problems also determine the values of the parameters ψ_d and ψ_r , showing the interdependence of all the complex phenomena involved during the formation and exfoliation of the graphene layers. In summary, the evolution of the carbon concentration is expressed as a function of four parameters: j_{C_0} , ψ_d , ψ_r and n , which are dependent on the temperature and gas composition used in each experiment. These dependences have been estimated by the following expressions:

$$j_{C_0} = \frac{k_C \cdot P_{CH_4}^{m_C}}{(1 + B_C \cdot P_{H_2})^2} \quad (9)$$

$$\psi_d = \frac{k_d \cdot P_{CH_4}^{m_d}}{1 + B_d \cdot P_{H_2}} \quad (10)$$

$$\psi_r = \frac{k_r \cdot P_{CH_4}^{m_r}}{1 + B_r \cdot P_{H_2}} \quad (11)$$

In order to ensure the convergence of the non-linear regression algorithm, the Arrhenius dependence with temperature for these kinetic parameters has been expressed on the basis of the reparametrized temperature, VT , as follows:

$$\begin{aligned} k_C &= k_{C_0} \cdot \exp(-E_C/RT) = k_{C_m} \cdot \exp(-E_C \cdot VT) \\ k_d &= k_{d_0} \cdot \exp(-E_d/RT) = k_{d_m} \cdot \exp(-E_d \cdot VT) \\ k_r &= k_{r_0} \cdot \exp(-E_r/RT) = k_{r_m} \cdot \exp(-E_r \cdot VT) \end{aligned} \quad (12)$$

The reparametrized temperature is given by:

$$VT = \frac{(T_m - T)}{R \cdot T_m \cdot T} \quad (13)$$

The reference temperature, T_m , used in this case for the parameter estimation is $T_m=1223$ K and the value of the Gas Constant is $R=0.008314$ kJ/mol·K. The calculation of the pre-exponential factors k_{C_0} , k_{d_0} and k_{r_0} shown in Table 3 is made using equation (12) after estimation of the apparent activation energies, E_C , E_d and E_r , and of k_{C_m} , k_{d_m} and k_{r_m} .

A power-law dependence with respect to the methane concentration and a pseudo-Langmuir-Hinshelwood dependence with respect to the H_2 partial pressure have been

assumed for the above expressions. For the temperature, an Arrhenius-type dependence is assumed, where E_C , E_d and E_r represent the apparent activation energies for each parameter, and k_{C0} , k_{d0} and k_{r0} are the corresponding pre-exponential factors.

The complete set of parameters has been estimated by non-linear least-squares multivariable regression of all the experimental data at the same time, using equations (7), (9), (10) and (11). The maximized objective function was the *Model Selection Criterion* (MSC) defined as [58,59]:

$$MSC = \ln \left(\frac{SST}{SSR} \right) - \left(\frac{2p}{n_p} \right) \quad (14)$$

In this equation, p represents the number of parameters and n_p the number of experimental points. The terms SST and SSR are the sum of total squares and the sum of the squared residuals, respectively. These terms are defined as:

$$SST = \sum_{i=1}^{i=n_p} \left(m_C^{\text{exp}} - \overline{m_C^{\text{exp}}} \right)^2 \quad (15)$$

$$SSR = \sum_{i=1}^{i=n_p} \left(m_C^{\text{exp}} - m_C^{\text{calc}} \right)^2 \quad (16)$$

One key advantage of the use of the MSC, unlike the SSR, is that it allows discrimination among several models with different numbers of parameters [60].

Figures 12a, 12b and 12c also include the model predictions together with the experimental data, showing a very high quality of the fitting. The values, standard errors and confidence intervals of each parameter are summarized in Tables 3 and 4. The low values of the standard error obtained for all the parameters confirm the goodness of the fitting attained with the kinetic model which is able to fit simultaneously the 11246 experimental data corresponding to the 14 curves presented in Figures 12a, 12b and 12c.

As regards the effect of the temperature, an increase of j_{C0} , ψ_d and ψ_r is observed in accordance with equations (9) to (11). From these expressions, the estimated value of the apparent activation energy for j_{C0} is 103.2 kJ/mol, which comes within the interval of the values published in the literature (80-130 kJ/mol) for the intrinsic growth rate of carbonaceous nanomaterials such as graphene or carbon nanotubes [61,62,63]. However, it should be noted that the values estimated for the apparent activation

energies, and for all the parameters in general, are strongly dependent on the kinetic model used, and therefore this type of comparison is always problematic. The values of both the pre-exponential factor and of the activation energy corresponding to the deactivation and regeneration parameters (see Table 3) indicate that the catalyst regeneration is more favoured by the increase in temperature than the deactivation phenomena, producing an increase in the residual reaction rate. Nevertheless, the value of the parameter n decreases with the temperature, from 0.86 at 850 °C until 0.48 at 975°C (see Table 4) indicating that the diffusional restrictions mentioned above are more significant as the temperature increases because the carbon content is higher. Obviously, the interdependence between these parameters ψ_r and n determine the final evolution of the catalyst activity. Furthermore, the increase in temperature causes a larger increment of j_{CO} than of ψ_d , both the pre-exponential factor and the activation energy are higher (see Table 2). This explains the increase in the initial reaction rate seen in Figure 12a.

As regards the effects of the increase in the partial pressure of methane, the orders of reactions estimated are 0.783 for j_{CO} and ψ_d , and 0.897 for ψ_r (see Table 2). Therefore, although the increase in the methane concentration in the feed does not modify the j_{CO}/ψ_d ratio, the greater value of k_{C_m} compared to k_{d_m} , explains the augmentation of the initial reaction rate shown in Figure 12b. The effect of the increase of ψ_r over the final reaction rate is modulated by the parameter n . In this case, the parameter n reaches a maximum value of 0.62 at 14.3% of CH₄, and then decreases until 0.46 at 42.9% of CH₄. Interestingly, this maximum coincides with the maximum in the I_{2D}/I_G ratio, which could indicate some relationship between both parameters.

Finally, with respect to the effects of the partial pressure of hydrogen, both j_{CO} , and ψ_d decrease as the %H₂ increases and ψ_r increases with the %H₂. This behaviour has been found in similar studies of catalytic hydrocarbon decomposition [25,26,32,33] and can be explained considering that the hydrogen inhibits both the growth and the deactivation process, due to the competitive adsorption between H₂ and CH₄ on the active sites of Ni-Cu nanoparticles. Simultaneously, the rise in the hydrogen concentration enhances the regeneration step but, as in the case of the temperature, causes a decrease in the parameter n .

In summary, the evolution of the carbon content is a consequence of the interplay of all the parameters involved, and of the relative variation of each parameter with the operating conditions. The kinetic model allows the relative importance of each variable to be discerned, and also provides some information about the impact of each of the stages - diffusion, deactivation and regeneration - involved during the carbon growth.

4. Conclusions

A biomorphic carbon (BC) supported Ni(40%)-Cu(8%) catalyst has been synthesized from cellulose using a one-step thermal decomposition method. This method allows obtaining a catalyst with a moderate surface area, 343 m²/g of area BET, a pore volume of 45 cm³/g and 33% microporosity, in which the Ni and Cu atoms are alloyed.

The Ni-Cu/BC catalyst has proved to be active in the synthesis of graphene and FLG by the catalytic decomposition of methane at temperatures around 950 °C. The characterization results have shown that the highest quality graphenic material is obtained operating at 950 °C with 28.6% of CH₄ and 14.3% of H₂. Under these conditions, the Raman spectra and TEM images have shown that the nanocarbonaceous material consists mainly of graphene and of 2 to 5 graphene layers (FLG). In addition, from the results obtained at different reaction times it has been ascertained that the formation of graphene in this type of catalyst occurs through the following steps: i) nucleation of a graphite layer covering the Ni-Cu metallic nanoparticles, ii) graphite exfoliation originating graphene and few layer graphene (FLG). This mechanism, combined with prior studies, was the basis used for the development of a phenomenological kinetic model that describes the growth of the carbonaceous nanomaterials described.

The results of this study indicate that nanocarbonaceous material productivity increases with the reaction temperature and the partial pressure of methane because the decomposition rate of methane increases under these operating conditions. This induces an increment in the carbon atoms dissolved in the metal nanoparticles, increasing the driving force through these nanoparticles. In contrast, an increment in the partial pressure of hydrogen produces a decrease in the amount of nanocarbonaceous material grown, caused by the competitive adsorption between H₂ and CH₄ on the active sites of Ni-Cu nanoparticles. The maximum carbon productivity, (0.0159 gC/gcat·min), is

obtained at 950 °C with 28.6% CH₄ and 0% H₂ in the feed. Combining both factors, productivity and quality, the optimum conditions for carrying out the reaction are 950 °C with 28.6% of CH₄ and 14.3% of H₂.

Finally, the results of the kinetic model indicate that the evolution of the carbon content is the consequence of the interplay of all the parameters involved, and of the relative variation of each parameter with the operating conditions. The model allows the relative importance of each one of the variables to be elucidated, and also provides information about the true impact of each of the stages involved during the carbon growth.

Acknowledgements.

The authors acknowledge financial support from MINECO (Madrid, Spain) FEDER, Project ENE2013-47880-C3-1-R.

-
- [1] X. Liu, L. Dai, *Nat. Rev. Mater.* 1 (2016) 1-11.
 - [2] Y. Yang, K. Chiang, N. Burke; *Catal. Today* 178 (2011) 197-205.
 - [3] E. Lam, J.H.T. Luong, *ACS Catal.* 4 (2014) 3393-3410.
 - [4] Ph. Sherp, J.L. Figueiredo, *Carbon Materials for Catalysis*, J. Willey and Sons. New Jersey 2009.
 - [5] S. Mann, *Biom mineralization: Principles and Concepts in Bioinorganic Materials Chemistry*, Oxford University Press, Oxford 2001.
 - [6] J. Will, C. Zollfrank, A. Kaindl, H. Sieber, P. Greil; *Keram. Z.* 62 (2010) 114-120.
 - [7] A. Zampieri, W. Schweiger, C. Zollfrank, P. Greil, in *Handbook of Biom mineralization*, (Ed: E. Baeuerlein), Wiley-VCH, Weinheim 2007.
 - [8] B. Bhushan, *Philos. Trans. R. Soc. A* 367 (2009) 1445-1486.
 - [9] O. Paris, I. Burgert, P. Fratzl; *MRS Bull.* 35 (2010) 219-225.
 - [10] T-X. Fan, S-K. Chow, D. Zhang, *Prog. Mat. Sci.* 54 (2009) 542-659.
 - [11] F. Cazaña, M.T. Jimaré, E. Romeo, V. Sebastián, S. Irusta, N. Latorre, C. Royo, A. Monzón, *Catal. Today* 249 (2015) 127-136.
 - [12] S. Ahmed, A. Aitani, F. Rahman, A. Al-Dawood, F. Al-Muhaish, *Appl. Catal. A-Gen.* 359 (2009) 1-24.
 - [13] A.M. Amin, E. Croiset, W. Epling, *Int J Hydrogen Energy* 36 (2011) 2904-2935.
 - [14] Y. Li, D. Li, G. Wang, *Catal. Today* 162 (2011) 1-48.

-
- [15] U.P.M. Ashik, W.M.A.W. Daud, H.F. Abbas, *Renew. Sust. Energ. Rev.* 44 (2015) 221-256.
- [16] A.C. Ferrari, J.C. Meyer, V. Scardaci, C. Casiraghi, M. Lazzeri, F. Mauri, S. Piscanec, D. Jiang, K.S. Novoselov, S. Roth, A.K. Geim, *Phys. Rev. Lett.* 97 (2006) 187401.
- [17] A.K. Geim, *Science* 324 (2009) 1530-1534.
- [18] K.S. Novoselov *Rev. Mod. Phys.* 83 (2011) 837-849.
- [19] R. Cheng, J. Bai, L. Liao, H. Zhou, Y. Chen, L. Liu, Y. Lin, S. Jiang, Y. Huang, X. Duan, *Proc. Natl. Acad. Sci. U. S. A.* 109 (2012) 11588-11592.
- [20] J. Shin, J.T. Kim, *Nanotechnology* 26 (2015) 365201.
- [21] N. Hu, Z. Yang, Y. Wang, L. Zhang, Y. Wang, X. Huang, H. Wei, L. Wei, Y. Zhang, *Nanotechnology* 25 (2014) 025502.
- [22] A.R. Siamaki, A.E.R.S. Khder, V. Abdelsayed, M.S. El-Shall, B.F. Gupton, *J. Catal.* 279 (2011) 1-11.
- [23] L. Ji, Z. Tan, T.R. Kuykendall, S. Aloni, S. Xun, E. Lin, V. Battaglia, Y. Zhang, *Phys. Chem. Chem. Phys.* 13 (2011) 7170-7177.
- [24] M.J. Nine, M.A. Cole, D.N.H. Tran, D. Losic, *J. Mater. Chem. A* 3 (2015) 12580-12602.
- [25] J.I. Villacampa, C. Royo, E. Romeo, J.A. Montoya, P. Del Angel, A. Monzón, *Appl. Catal., A* 252 (2003) 363-383.
- [26] M. Pérez-Cabero, E. Romeo, C. Royo, A. Monzón, A. Guerrero-Ruiz, I. Rodríguez-Ramos, *J. Catal.* 224 (2004) 197-205.
- [27] De Chen; K.O. Christensen, E. Ochoa-Fernández, Z. Yu, B. Tøtdal, N. Latorre, A. Monzón, A. Holmen, *J. Catal.* 229 (2005) 82-96.
- [28] L. Dussault, J.C. Dupin, C. Guimon, M. Monthieux, N. Latorre, T. Ubieta, E. Romeo, C. Royo, A. Monzón, *J. Catal.* 251 (2007) 223-232.
- [29] A. Monzon, G. Lolli, S. Cosma, S. B. Mohamed, and D. E. Resasco, *J. Nanosci. Nanotechno.* 8 (2008) 6141-6152.
- [30] P. Benito, M. Herrero, F.M. Labajos, V. Rives, C. Royo, N. Latorre, A. Monzón, *Chem. Eng. J.* 149 (2009) 455-462.
- [31] N. Latorre, E. Romeo, F. Cazaña, T. Ubieta, C. Royo, J. I. Villacampa, A. Monzón, *J. Phys. Chem. C* 114 (2010) 4773-4782.

-
- [32] E. Romeo, M. Saeys, A. Monzón, A. Borgna; *Int. J. Hydrogen Energ.* 39, 31 (2014) 18016-18026.
- [33] N. Latorre, J.I. Villacampa, T. Ubieta, E. Romeo, C. Royo, A. Borgna, A. Monzon, *Top. Catal.* 51 (2008) 158-168
- [34] S. Bhaviripudi, X. Jia, M.S. Dresselhaus, J. Kong, *Nano Lett.* 10 (2010) 4128-4133.
- [35] L. Dussault, J.C. Dupin, N. Latorre, T. Ubieta, L. Noé, M. Monthieux, E. Romeo, C. Royo, A. Monzon, C. Guimon. *J. Phys. Chem. Solids* 67 (2006) 1162-1167.
- [36] M. M. Dubinin, L. V. Radushkevich, *Proc. Acad. Sci. USSR* 55 (1947) 331-333.
- [37] J. Biscoe, B.E. Warren, *J. Appl. Phys.* 13 (1942) 364-371.
- [38] C. Botas, P. Álvarez, C. Blanco, R. Santamaría, M. Granda, M.D. Gutiérrez, F. Rodríguez-Reinoso, R. Menéndez, *Carbon* 52 (2013) 476-485.
- [39] D. Torres, J.L. Pinilla, R. Moliner, I. Suelves, *Carbón* 81 (2015) 405-417.
- [40] K.S.W. Sing, D.H. Everett, R.A.W. Haul, L. Moscou, R.A. Pierotti, J. Rouquerol, T. Siemieniewska, *Pure Appl. Chem.* 57 (1985) 603-619.
- [41] S. Lowell, J. Shields, M.A. Thomas, M. Thommes, *Characterization of Porous Solids and Powders: Surface Area Pore Size and Density*, The Netherlands, Springer, Dordrecht, 2006.
- [42] Q. Wu, L.D.L. Duchstein, G.L. Chiarello, J.M. Christensen, C.D. Damsgaard, C.F. Elkjaer, J.B. Wagner, B. Temel, J. Grunwaldt, A.D. Jensen, *ChemCatChem.* 6 (2014) 301-310.
- [43] H.W. King, *J. Mater. Sci.* 1 (1966) 79-90.
- [44] L. Lua, V. Sahajwalla, C. Kong and D. Harris, *Carbon* 39 (2001) 1821-1833.
- [45] L. Ma, X. Zhang, D. Lin, Y. Chun, Q. Xu, *Appl. Catal. A* 460-461 (2013) 26-35.
- [46] Y-R. Rhim, D. Zhang, D. H. Fairbrother, K. A. Wepasnick, K. J. Livi, R. J. Bodnar, D. C. Nagle, *Carbon* 48 (2010) 1012-1024.
- [47] A.C. Ferrari, J. Robertson, *Phys. Rev. B* 61, (2000) 14095-14107.
- [48] A. C. Ferrari, D. M. Basko, *Nat. Nanotechnol.* 8 (2013) 235-246.
- [49] L.M. Malard, M.A. Pimenta, G. Dresselhaus, M.S. Dresselhaus, *Phys. Rep.* 473 (2009) 51-87
- [50] Y. Hao, Y. Wang, L. Wang, Z. Ni, Z. Wang, R. Wang, C.K. Koo, Z. Shen, J.T.L. Thong, *Small* 6 (2) (2010) 195-200.

-
- [51] C. Cong, T. Yu, R. Saito, G.F. Dresselhaus, M.S. Dresselhaus, ACS Nano 5 (3) (2011) 1600-1605.
- [52] Z.H Ni, Y.Y. Wang, T. Yu, Y. You, Z.X. Shen, Phys. Rev. B 77 (2008) 235403.
- [53] J.C. Rodríguez, J.A. Peña, A. Monzón, R. Hughes, K. Li, Chem. Eng. J. 58 (1995) 7-13.
- [54] A. Monzón, E. Romeo, A. Borgna, Chem. Eng. J. 94 (2003) 19-28.
- [55] J. Corella, J. Adanez, A. Monzón, Ind. Eng. Chem. Res. 27(3) (1988) 375-381.
- [56] I. J. Alstrup, J. Catal. 109 (1988) 241-251.
- [57] C. I. Meyer, A. J. Marchi, A. Monzon, T. F. Garetto; Appl. Catal. A: General, 367 (1-2) (2009) 122-129.
- [58] S. Sclove, Psychometrika 52 (1987) 333-343.
- [59] M S Software, Statistical Analysis, Micromath, Salt Lake City, USA, 1995.
- [60] S. Armenise, E. Garcia-Bordeje, J.L. Valverde, E. Romeo and A. Monzon, Phys. Chem. Chem. Phys. 15 (2013) 12104-12117.
- [61] Y. Lee, J. Park, Y. Choi, H. Ryu, H. Lee, J Phys Chem B. 106 (2002) 7614-7618.
- [62] H. Mehdipour, K. Ostrikov, ACS Nano. 6 (2012) 10276-10286.
- [63] J. Li, E. Croiset, L. Ricardez-Sandoval, J. Catal. 326 (2015) 15-25.

Table 1. Textural properties of fresh Ni-Cu/BC catalyst and of the carbonaceous nanomaterials obtained at different reaction temperatures.

	BET surface (m²/g)	Pore volume (cm³/g)	Micropore volume (cm³/g)	% Micropore volume
<i>Ni-Cu/BC fresh</i>	343	0.451	0.148	32.9
<i>Reaction: 900 °C</i>	40	0.140	0.019	13.7
<i>Reaction: 950 °C</i>	24	0.101	0.011	11.0
<i>Reaction: 975 °C</i>	21	0.075	0.009	12.4

Table 2. Influence of the operating conditions on the I_G/I_D and I_{2D}/I_G ratios.

Temperature (°C)	I_G/I_D	I_{2D}/I_G
<i>fresh</i>	<i>1.03</i>	<i>0</i>
<i>850</i>	<i>3.31</i>	<i>0.40</i>
<i>900</i>	<i>2.56</i>	<i>0.53</i>
<i>925</i>	<i>2.20</i>	<i>0.59</i>
<i>950</i>	<i>2.84</i>	<i>0.92</i>
<i>975</i>	<i>1.00</i>	<i>0.69</i>
pCH₄ (bar)	I_G/I_D	I_{2D}/I_G
<i>1.4</i>	<i>1.26</i>	<i>0.51</i>
<i>7.1</i>	<i>6.50</i>	<i>0.73</i>
<i>14.3</i>	<i>3.69</i>	<i>1.68</i>
<i>28.6</i>	<i>2.84</i>	<i>0.92</i>
<i>42.9</i>	<i>1.57</i>	<i>0.52</i>
pH₂ (bar)	I_G/I_D	I_{2D}/I_G
<i>0.0</i>	<i>1.16</i>	<i>0.40</i>
<i>7.1</i>	<i>1.59</i>	<i>0.72</i>
<i>14.3</i>	<i>2.84</i>	<i>0.92</i>
<i>28.6</i>	<i>4.38</i>	<i>0.82</i>
Time (min)	I_G/I_D	I_{2D}/I_G
<i>0</i>	<i>1.03</i>	<i>0</i>
<i>1</i>	<i>1.38</i>	<i>0.24</i>
<i>4</i>	<i>1.70</i>	<i>0.63</i>
<i>120</i>	<i>2.84</i>	<i>0.92</i>

Table 3. Parameters of the Kinetic Model of Carbon Growth.

Parameter	Value	Standard Error	L.L. (95%)	U.L. (95%)
k_{C_0} (gC/bar ^{mc} ·gcat·min)	0.582	0.003	0.576	0.589
j_{C_0}				
E_c (kJ/mol)	103.3	0.3	102.8	103.8
m_c	0.783	0.004	0.776	0.791
B_c (bar ⁻¹)	0.11	0.01	0.10	0.12
k_{d_0} (gC/bar ^{md} ·gcat·min)	0.420	0.004	0.412	0.427
ψ_d				
E_d (kJ/mol)	45.1	0.6	43.9	46.3
m_d	0.782	0.007	0.769	0.795
B_d (bar ⁻¹)	0.89	0.03	0.84	0.95
k_{r_0} (gC/bar ^{mr} ·gcat·min)	0.407	0.008	0.393	0.422
ψ_r				
E_r (kJ/mol)	145.3	0.8	143.7	146.9
m_r	0.893	0.013	0.867	0.919
B_r (bar ⁻¹)	-0.81	0.02	-0.85	-0.78

MSC = 7.936; $R^2 = 0.9996$; Significance level $\alpha = 0.05$

Table 4. Values of the kinetic model parameter n obtained. Influence of the operating conditions.

Temperature (°C)	n
<i>850</i>	<i>0.86</i>
<i>900</i>	<i>0.66</i>
<i>925</i>	<i>0.59</i>
<i>950</i>	<i>0.53</i>
<i>975</i>	<i>0.48</i>
pCH₄ (bar)	n
<i>1.4</i>	<i>0.61</i>
<i>7.1</i>	<i>0.61</i>
<i>14.3</i>	<i>0.62</i>
<i>28.6</i>	<i>0.53</i>
<i>42.9</i>	<i>0.46</i>
pH₂ (bar)	n
<i>0.0</i>	<i>0.63</i>
<i>7.1</i>	<i>0.59</i>
<i>14.3</i>	<i>0.53</i>
<i>28.6</i>	<i>0.48</i>

Figure captions

Figure 1. N₂ adsorption and desorption isotherms of Ni-Cu/BC catalyst after preparation and reaction at 900, 950 and 975 °C.

Figure 2. XRD pattern of fresh Ni-Cu/BC catalyst and after reaction at 950 °C, 28.6% CH₄, 14.3% H₂, 57.1% N₂ at different reaction times.

Figure 3. a) SEM and b) TEM images of fresh Ni-Cu/BC catalyst.

Figure 4. a) Raman spectra of Ni-Cu/BC fresh catalyst, and after reaction at different temperatures. Feed composition: 28.6% CH₄, 14.3% H₂, 57.1% N₂. b) Deconvolution of the 2D band after reaction at 900 and 950 °C.

Figure 5. TEM images of Ni-Cu/BC catalyst after reaction at a) 900 °C; and b) 950 °C. Feed composition: 28.6% CH₄, 14.3% H₂, 57.1% N₂.

Figure 6. Raman spectra obtained after reaction at 950 °C and with 14.3% H₂. Influence of the partial pressure of methane.

Figure 7. TEM images after reaction at 950 °C and with 14.3% H₂. Influence of the partial pressure of methane. a) 7.1% CH₄, b) 28.6% CH₄, c) 42.9% CH₄.

Figure 8. Raman spectra acquired after reaction at 950 °C and with 28.6% CH₄. Influence of the partial pressure of hydrogen.

Figure 9. TEM images after CCVD reaction at 950 °C and with 28.6% CH₄. Influence of the partial pressure of hydrogen. a) 0% H₂, b) 14.3% H₂.

Figure 10. Raman signal for Ni-Cu/BC catalyst after CCVD reaction at 950 °C with 28.6% CH₄ and 14.3% H₂. Influence of the reaction time.

Figure 11. TEM images of Ni-Cu/BC catalyst after CCVD reaction at 950 °C with 28.6% CH₄ and 14.3% H₂ during a) 1 min, b) 4 min and c) 120 min.

Figure 12. Evolution of carbon concentration, gC/gcat. over time. Influence of: a) reaction temperature; b) % CH₄ and c) % H₂. Dashed red line: model prediction.

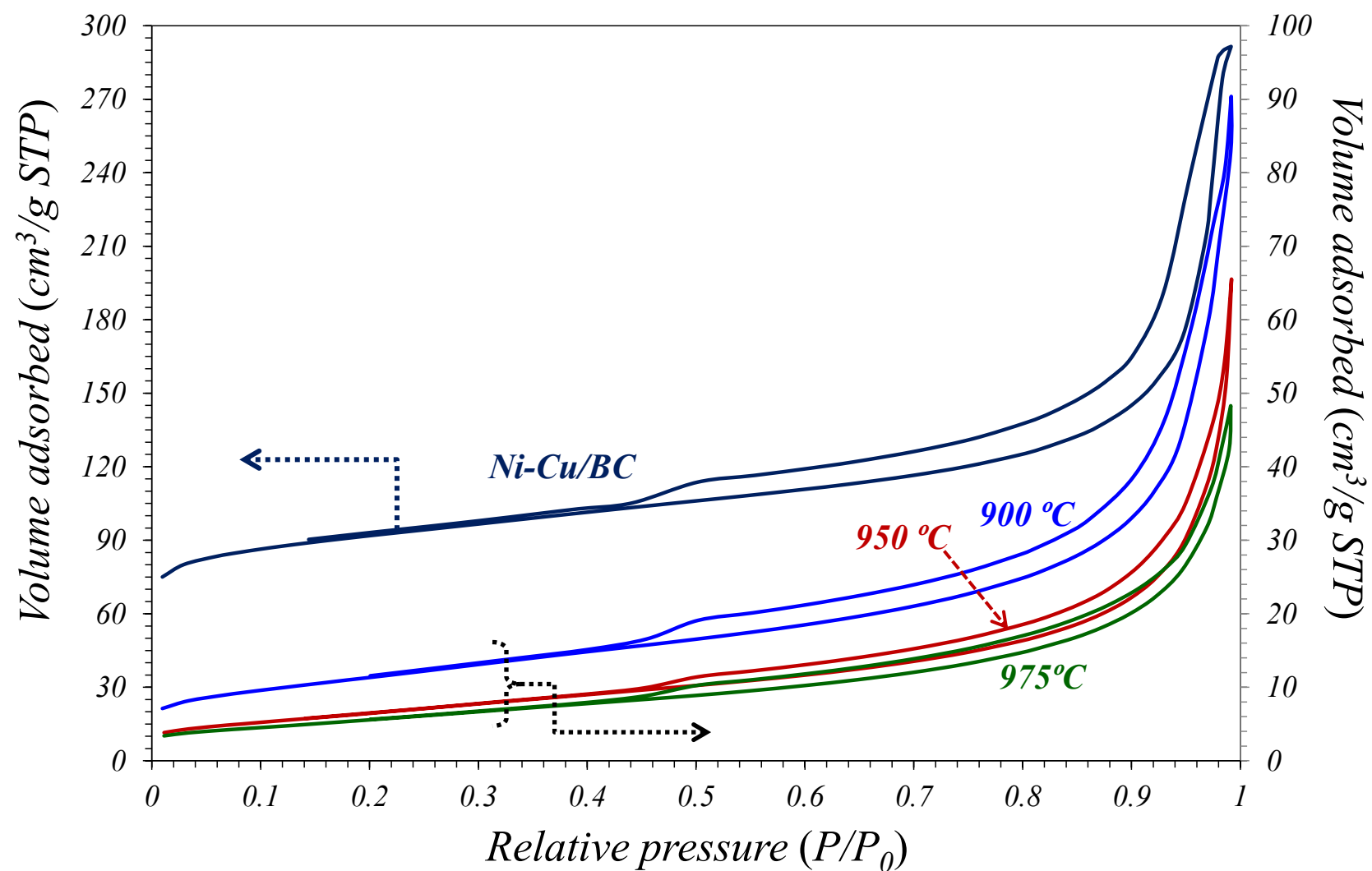


Figure 1

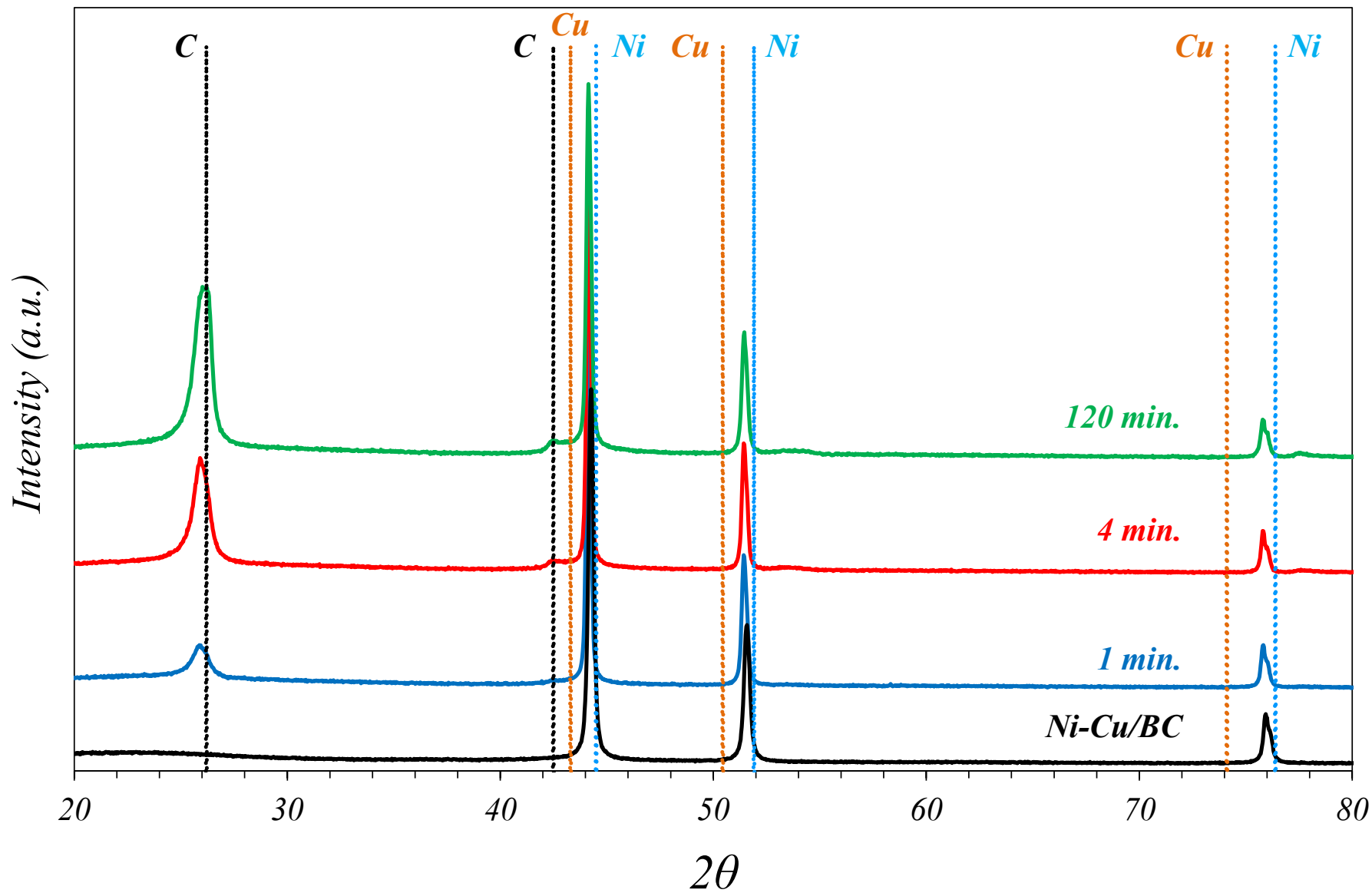


Figure 2

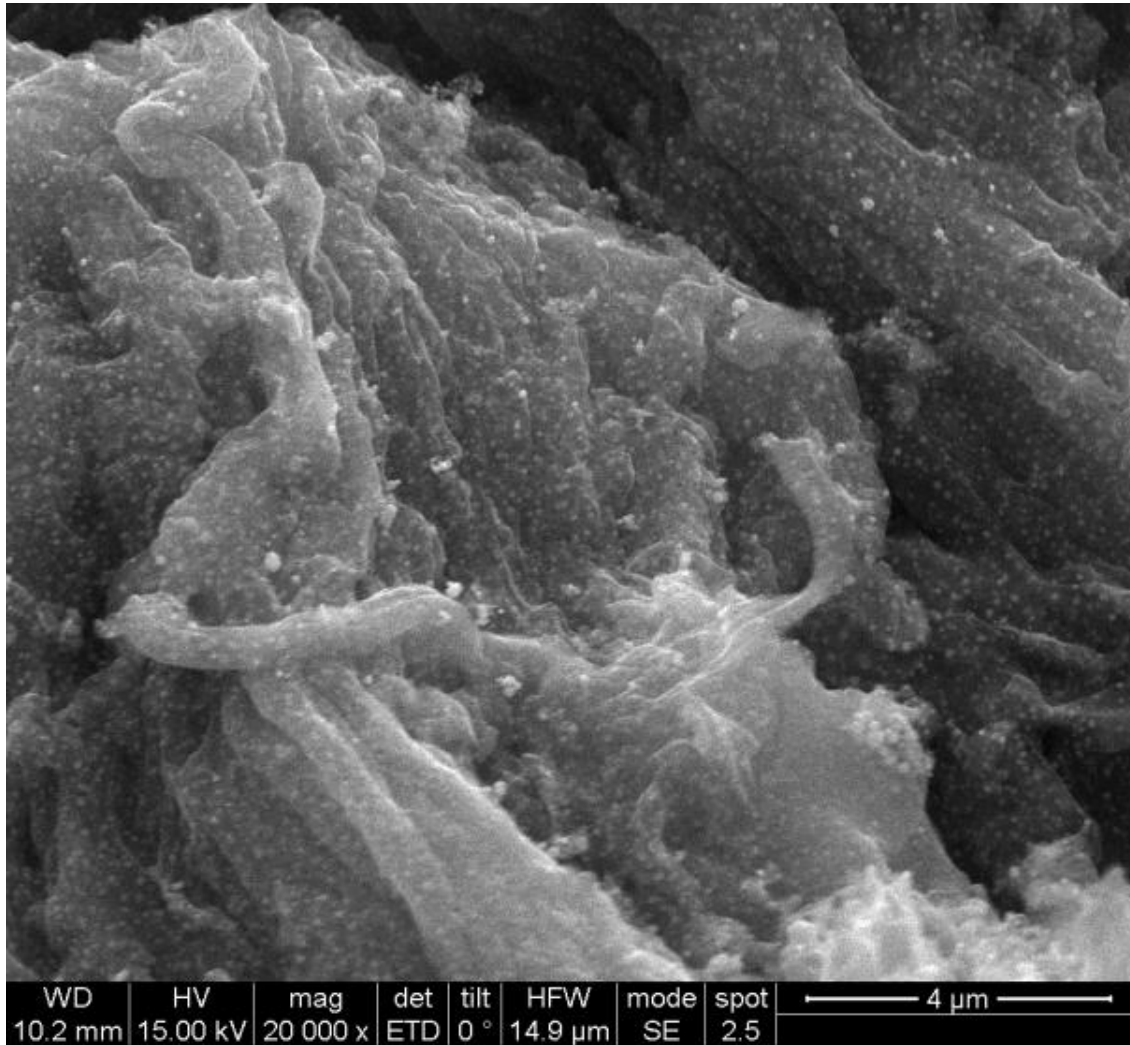


Figure 3a

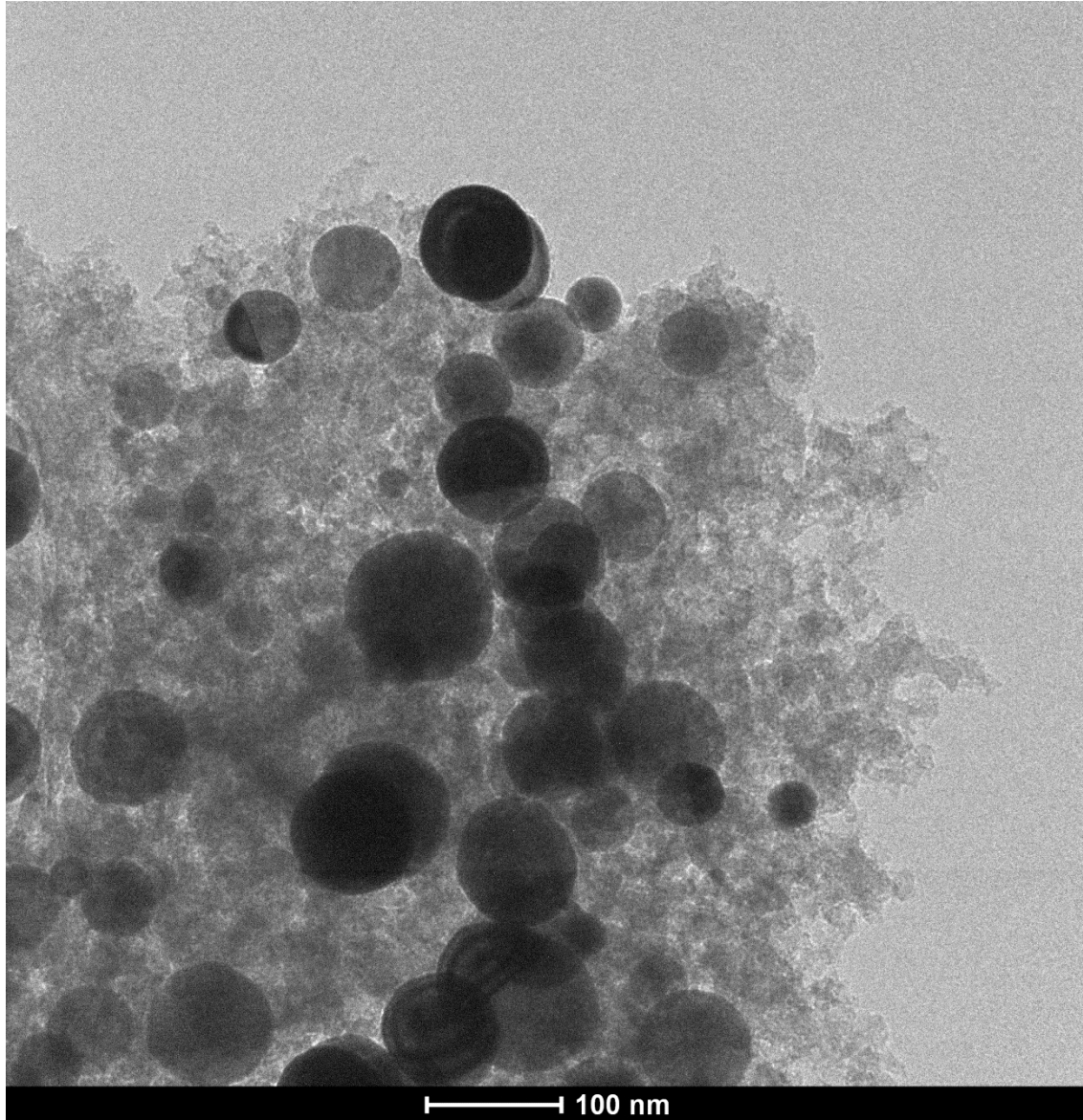


Figure 3b

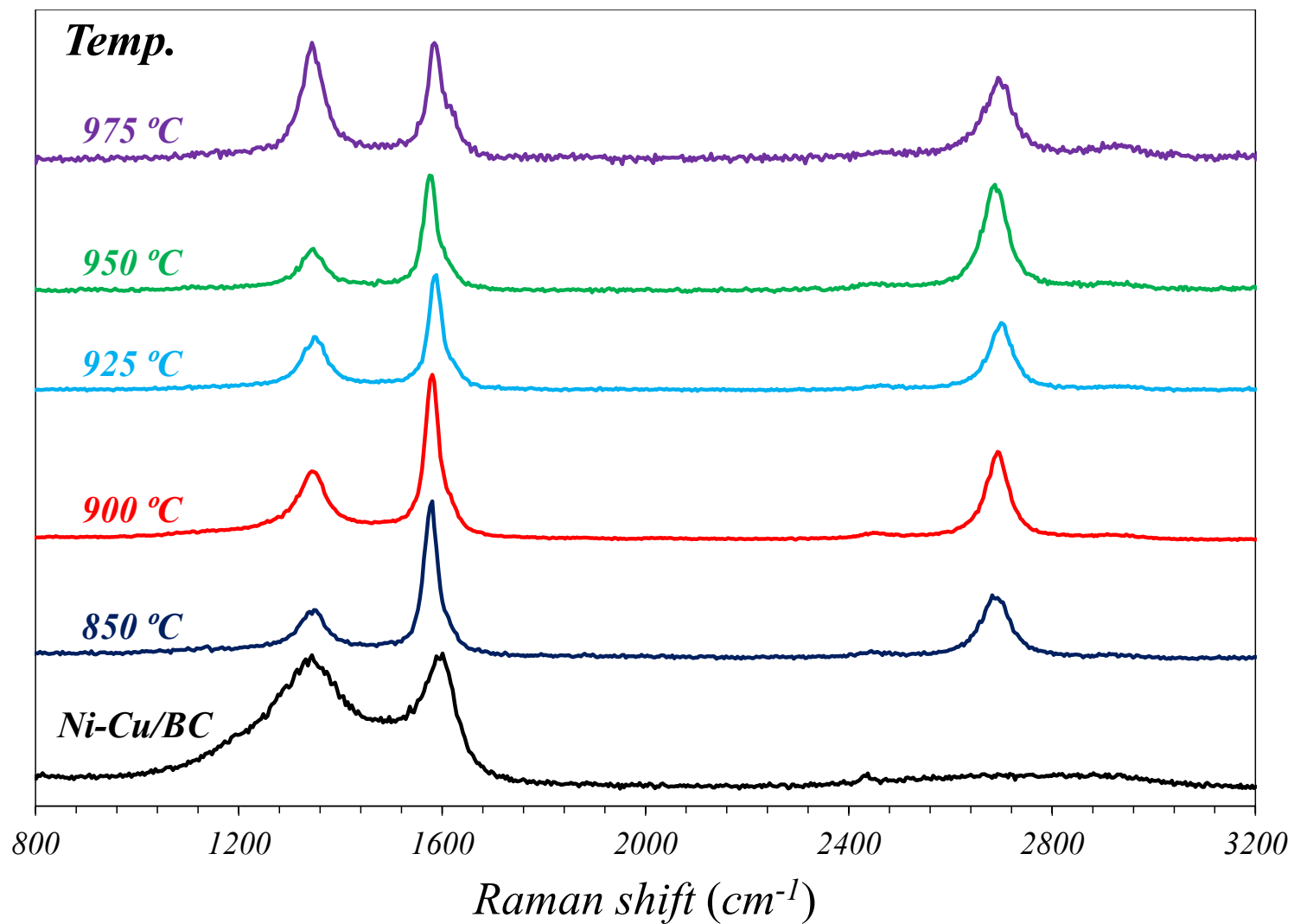


Figure 4a

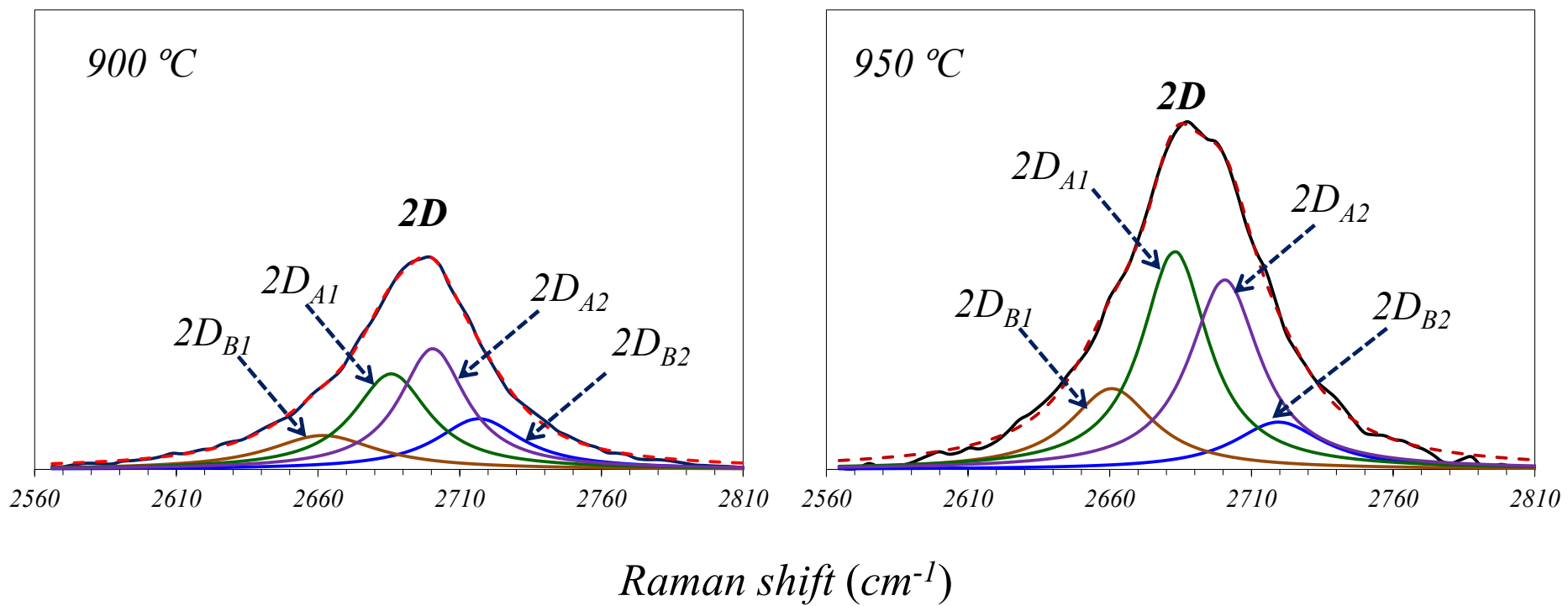


Figure 4b

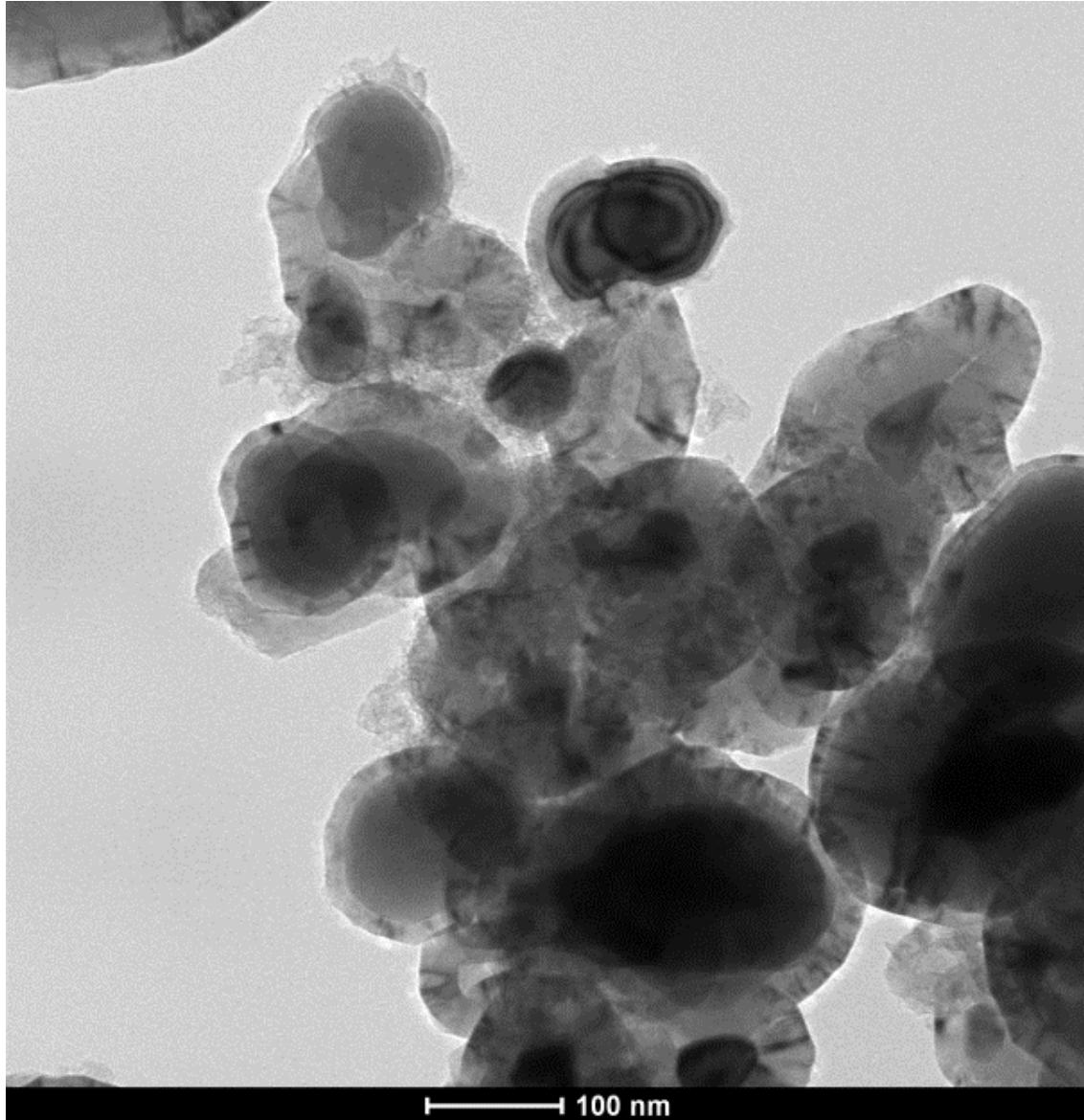


Figure 5a

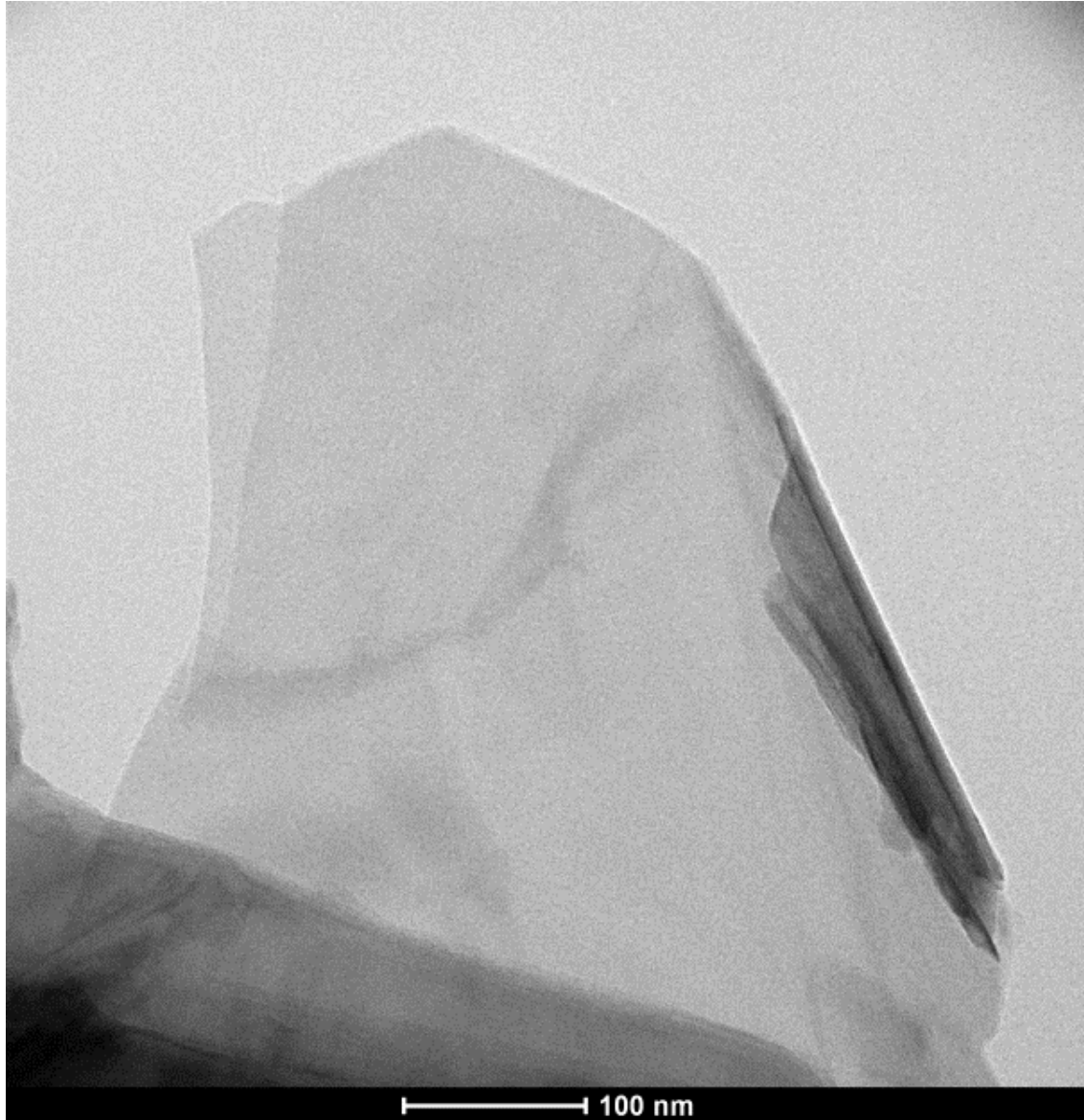


Figure 5b

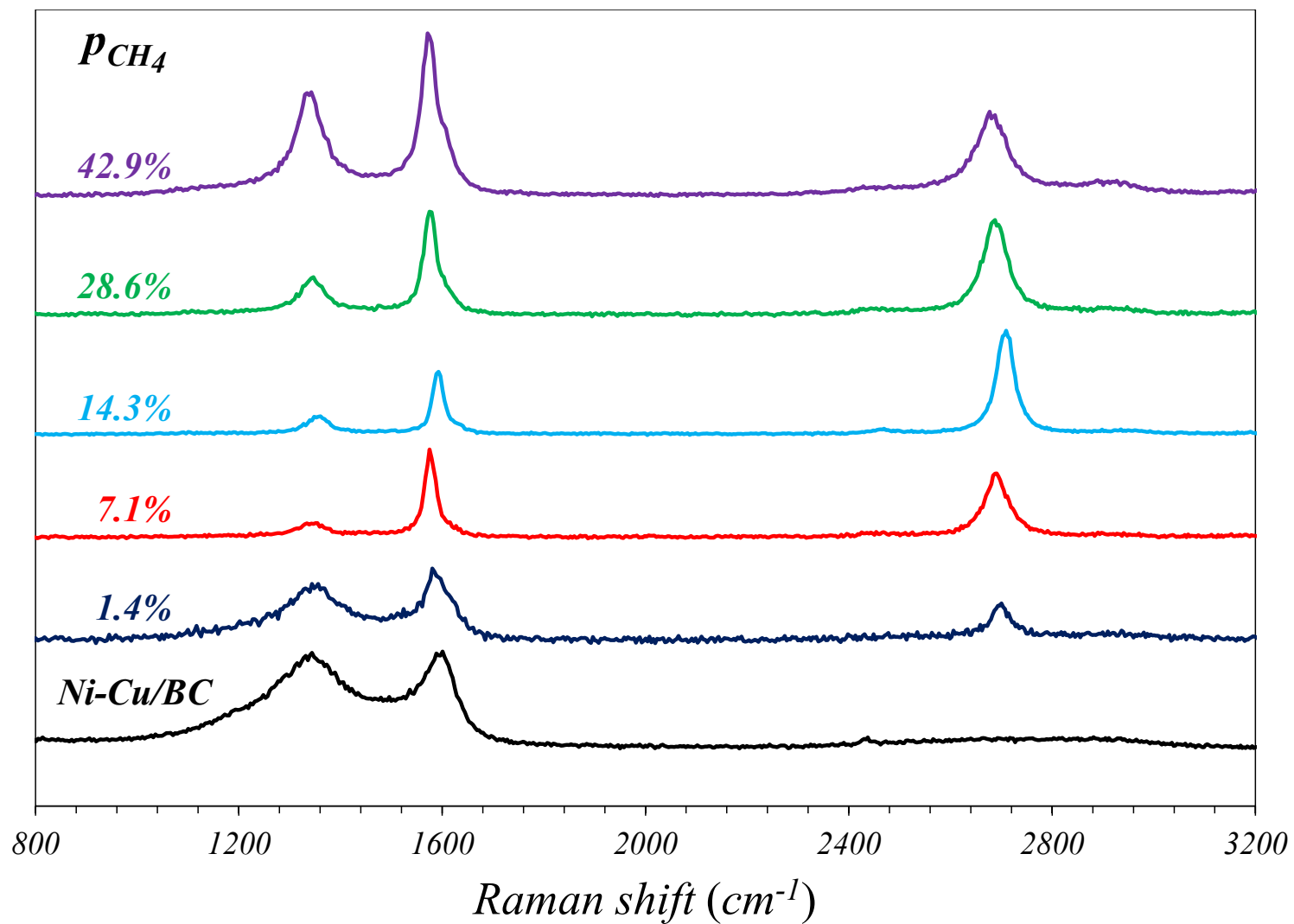


Figure 6

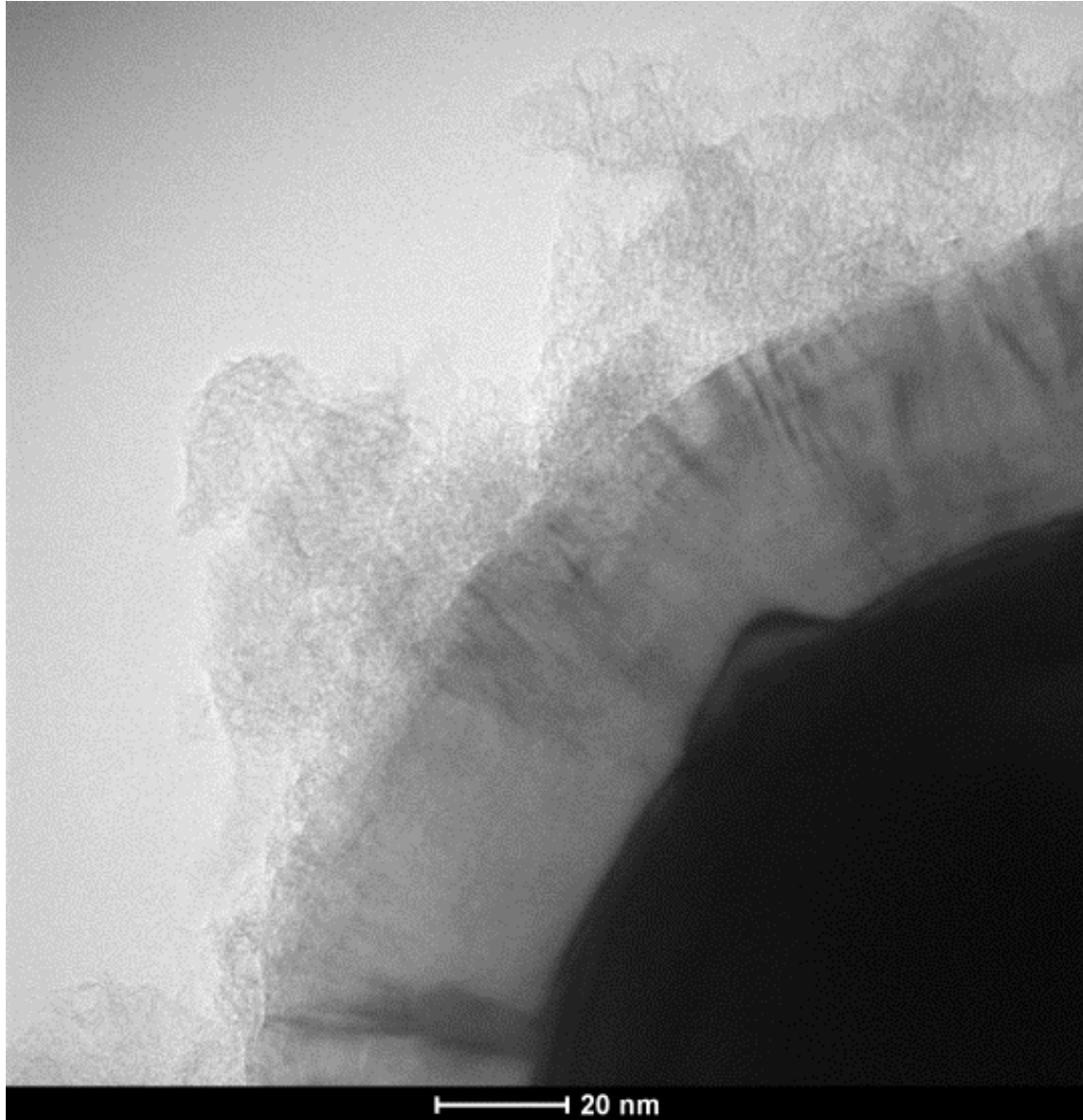


Figure 7a



Figure 7b

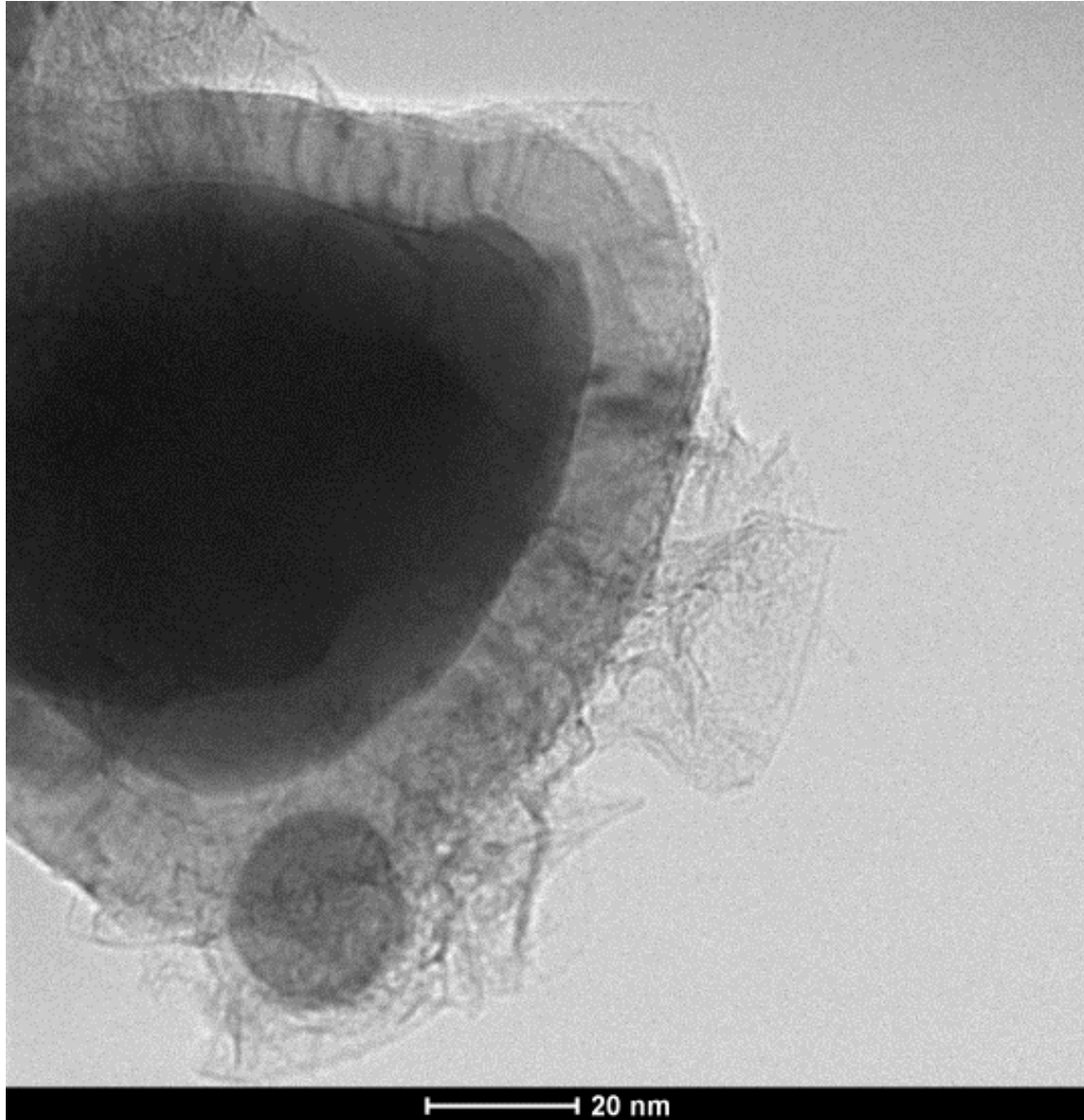


Figure 7c

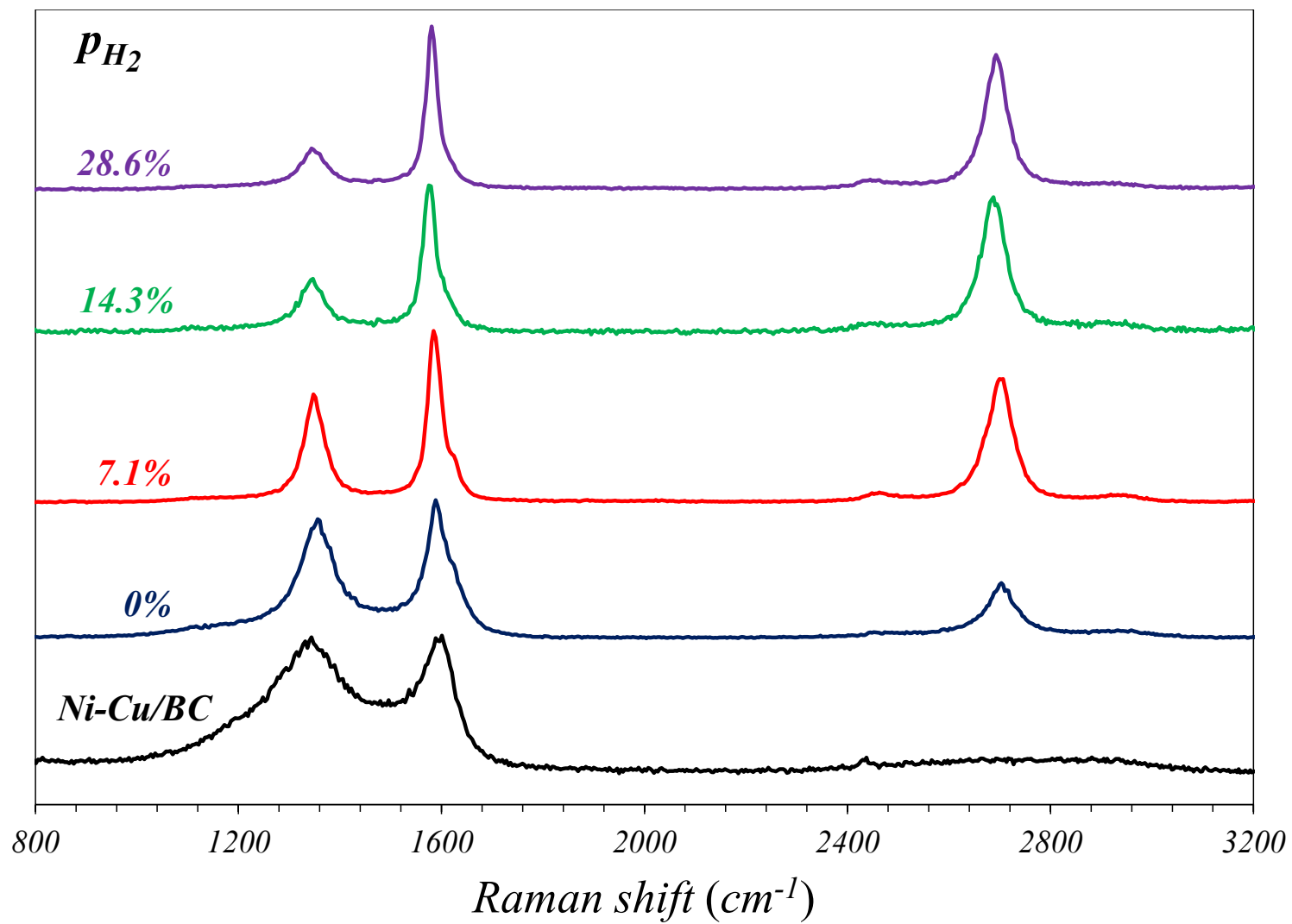


Figure 8

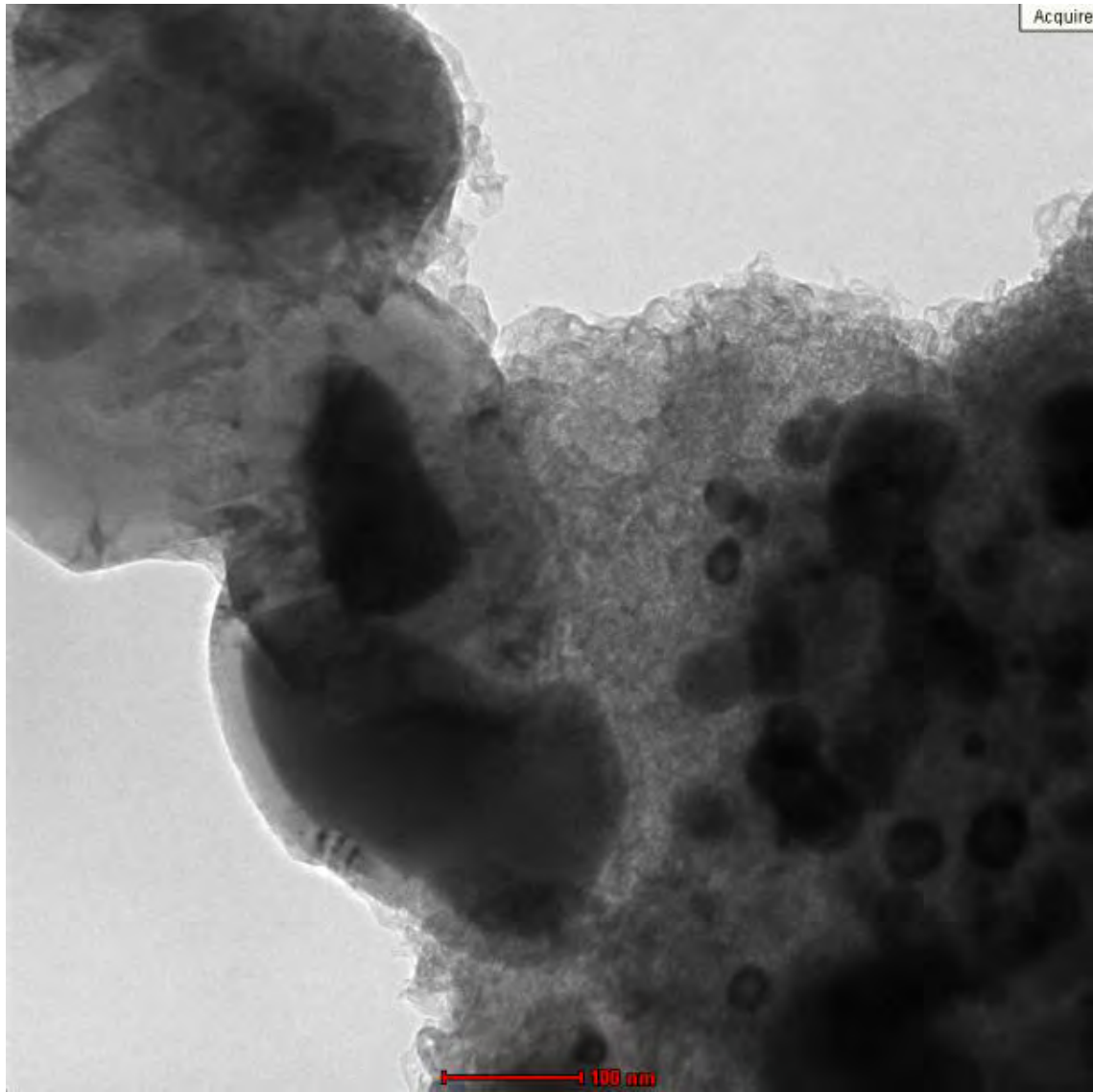


Figure 9a



Figure 9b

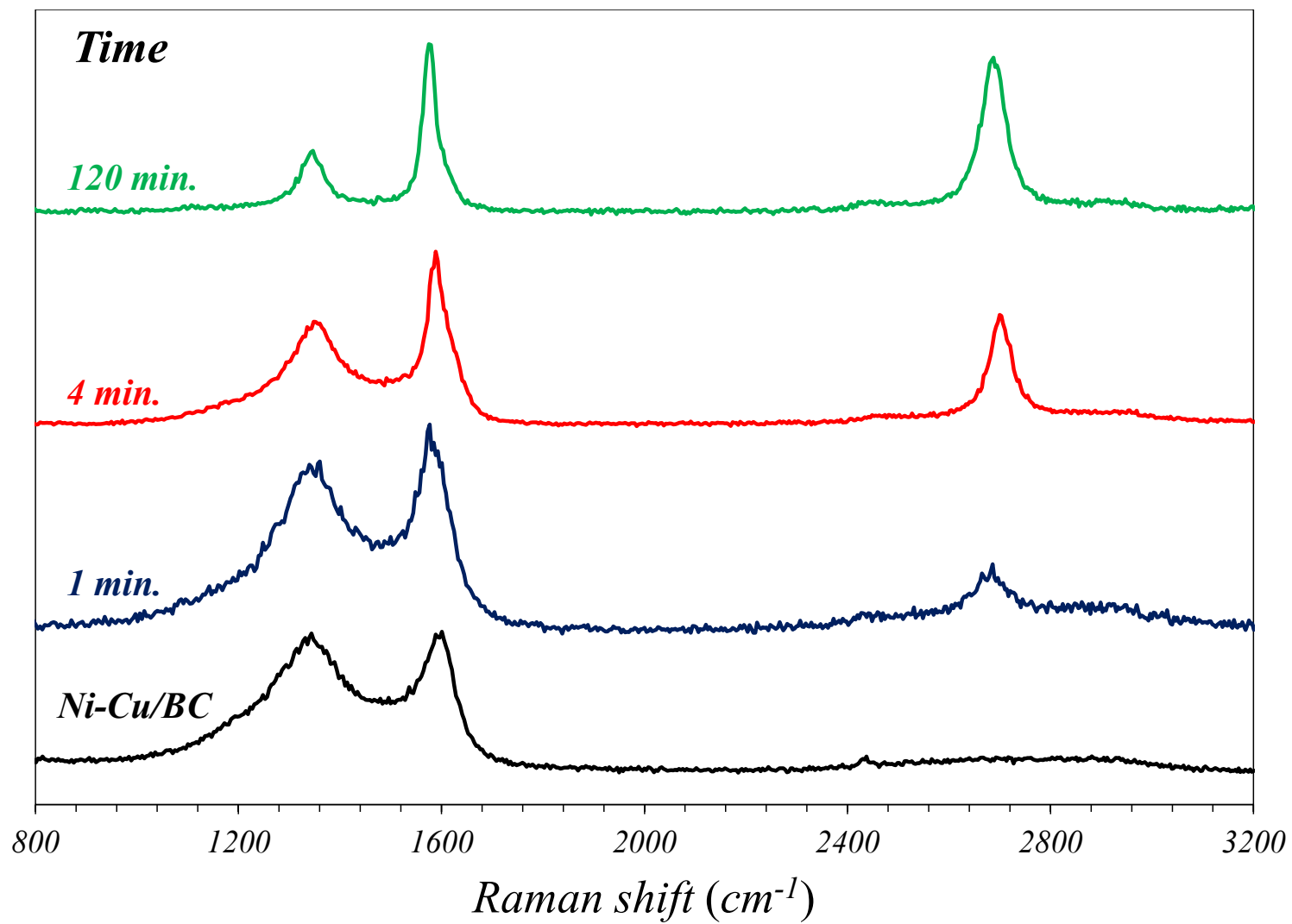


Figure 10

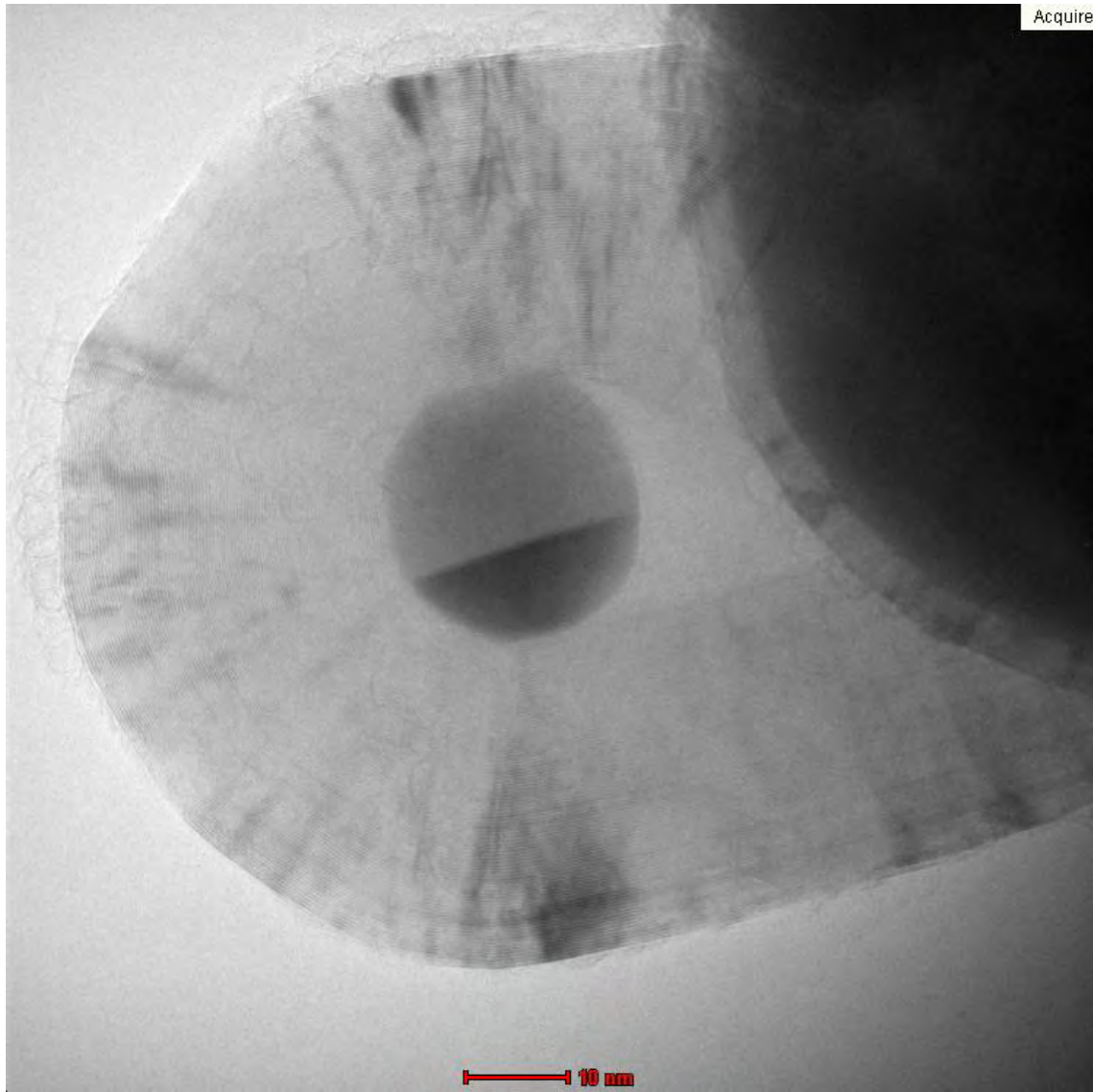


Figure 11a



Figure 11b

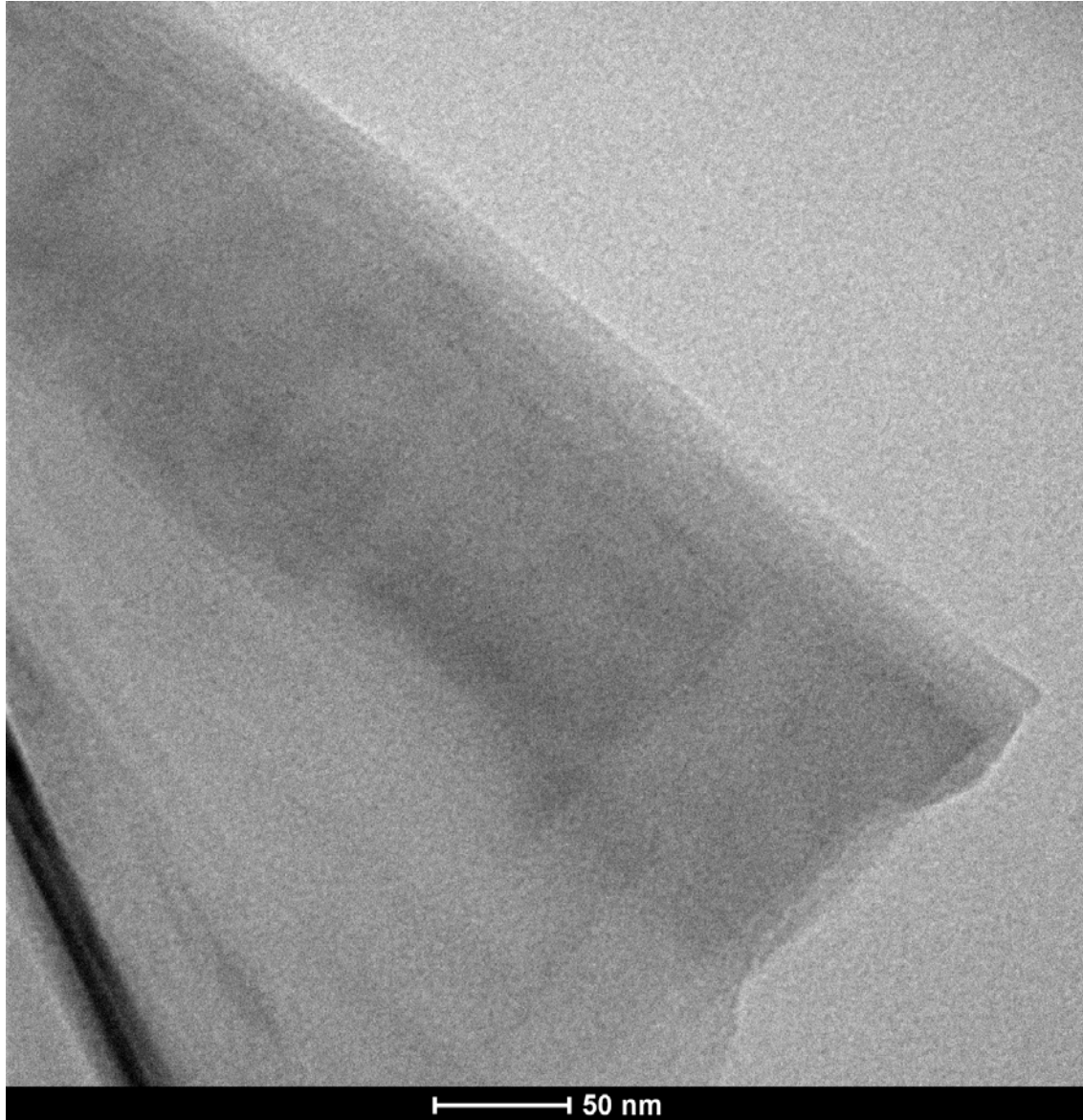


Figure 11c

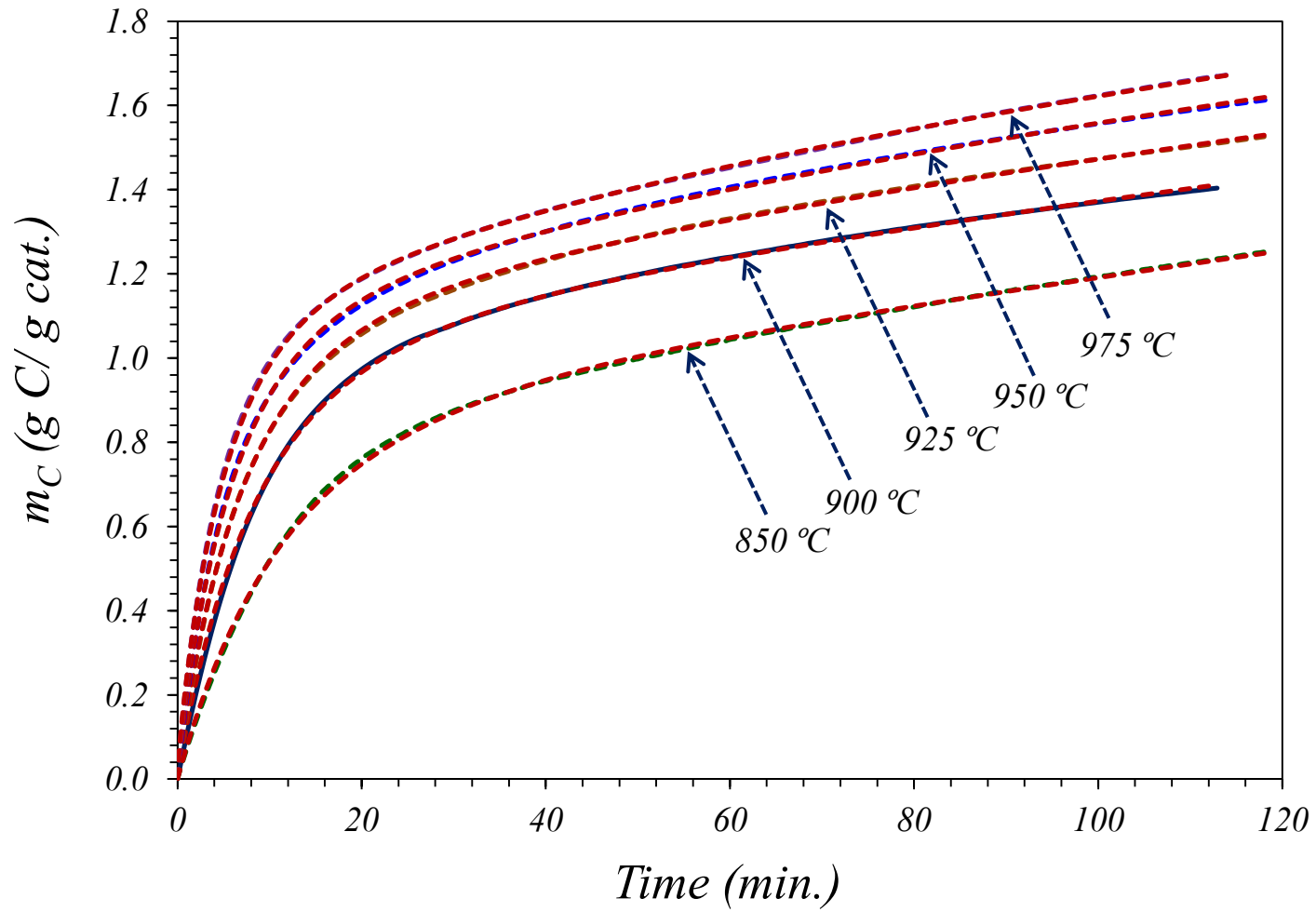


Figure 12a

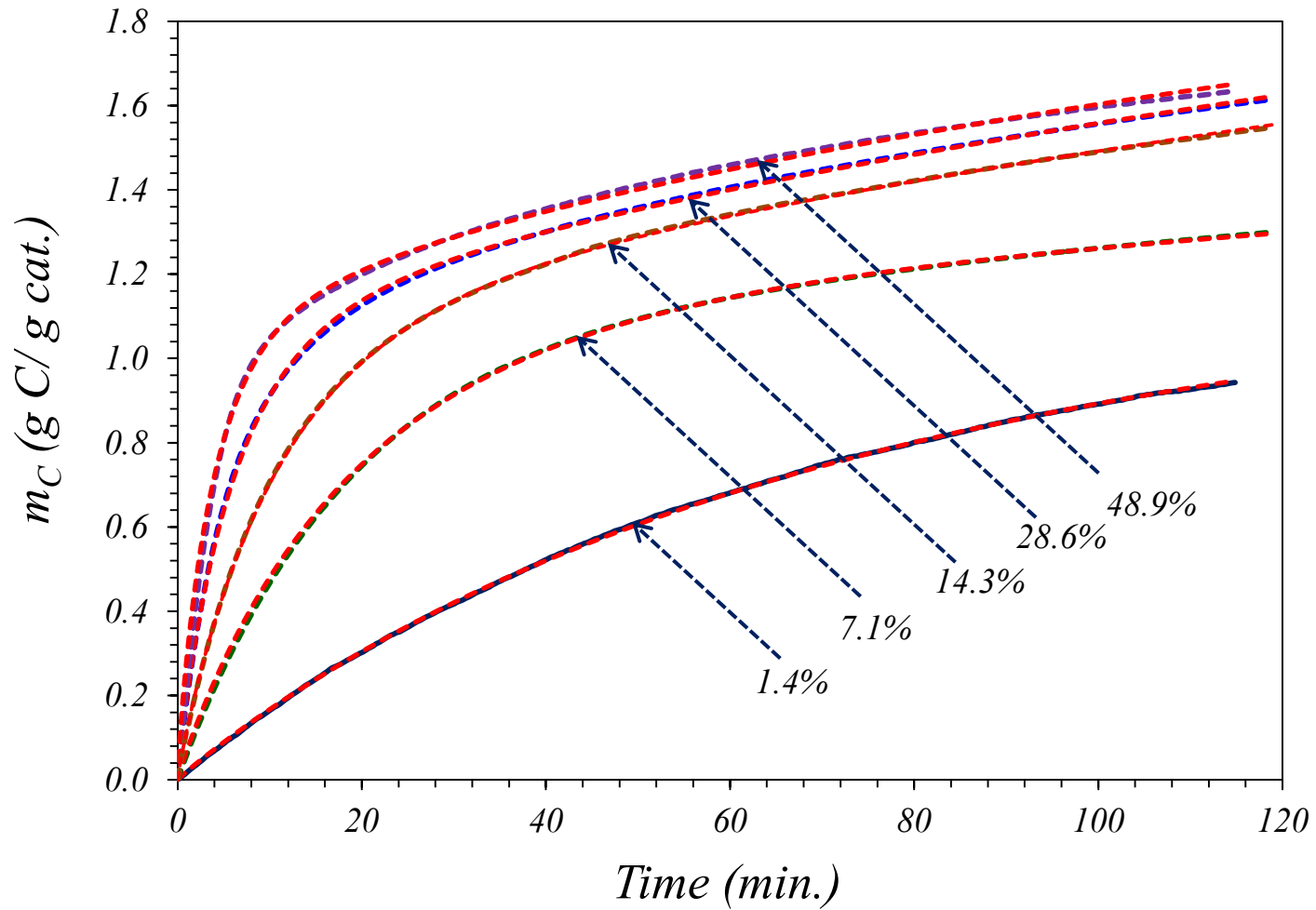


Figure 12b

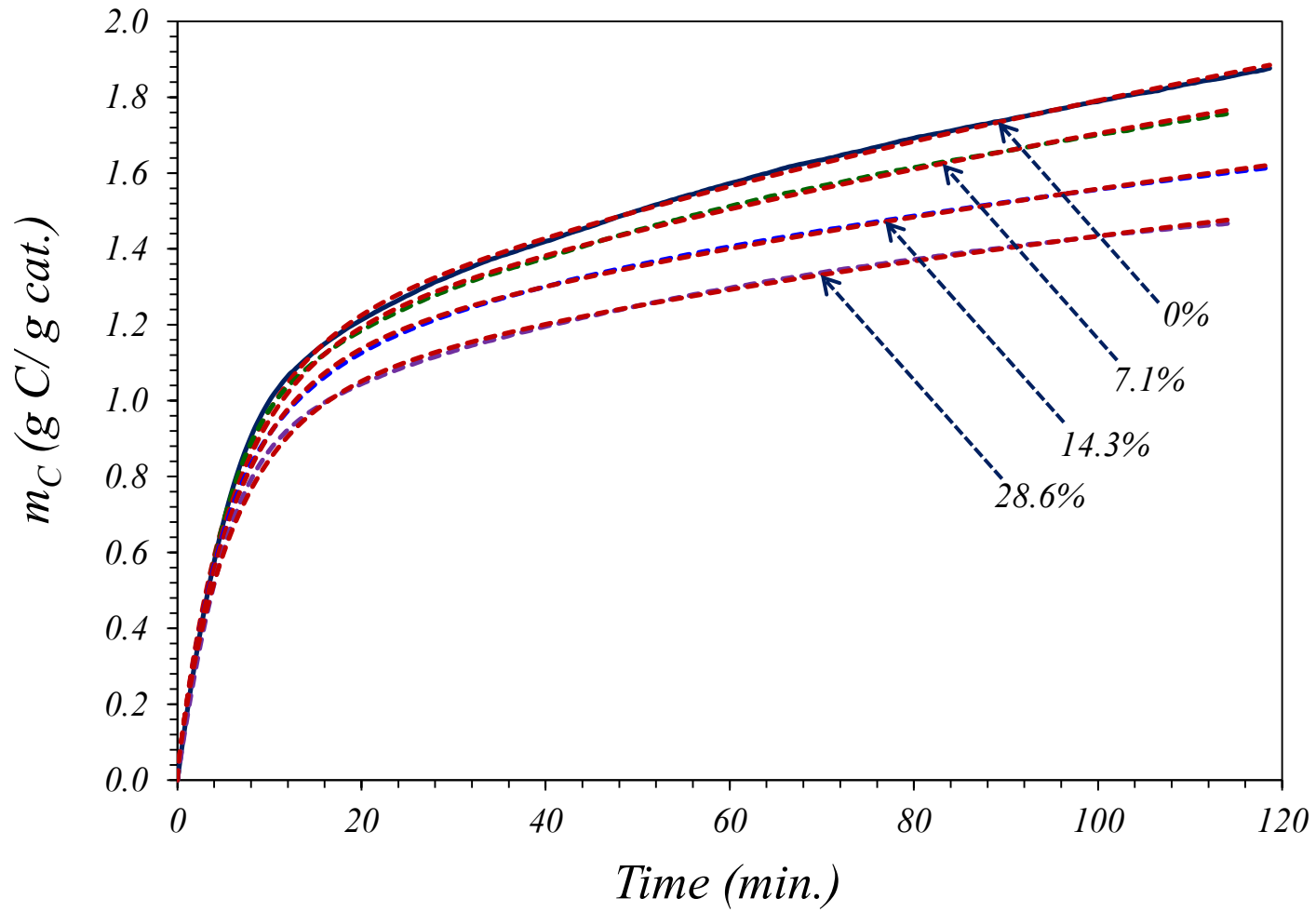


Figure 12c